



Published in final edited form as:

J Comput Phys. 2007 December 10; 227(2): 1046–1074. doi:10.1016/j.jcp.2007.08.021.

A Kernel-free Boundary Integral Method for Elliptic Boundary Value Problems *

Wenjun Ying* and

Departments of Mathematics and Biomedical Engineering, Duke University, Durham, NC 27708-0281, USA

Craig S. Henriquez

Department of Biomedical Engineering, Duke University, Durham, NC 27708-0281, USA

Abstract

This paper presents a class of kernel-free boundary integral (KFBI) methods for general elliptic boundary value problems (BVPs). The boundary integral equations reformulated from the BVPs are solved iteratively with the GMRES method. During the iteration, the boundary and volume integrals involving Green's functions are approximated by structured grid-based numerical solutions, which avoids the need to know the analytical expressions of Green's functions. The KFBI method assumes that the larger regular domain, which embeds the original complex domain, can be easily partitioned into a hierarchy of structured grids so that fast elliptic solvers such as the fast Fourier transform (FFT) based Poisson/Helmholtz solvers or those based on geometric multigrid iterations are applicable. The structured grid-based solutions are obtained with standard finite difference method (FDM) or finite element method (FEM), where the right hand side of the resulting linear system is appropriately modified at irregular grid nodes to recover the formal accuracy of the underlying numerical scheme. Numerical results demonstrating the efficiency and accuracy of the KFBI methods are presented. It is observed that the number of GMRES iterations used by the method for solving isotropic and moderately anisotropic BVPs is independent of the sizes of the grids that are employed to approximate the boundary and volume integrals. With the standard second-order FEMs and FDMs, the KFBI method shows a second-order convergence rate in accuracy for all of the tested Dirichlet/Neumann BVPs when the anisotropy of the diffusion tensor is not too strong.

Keywords

elliptic equation; anisotropy; kernel-free boundary integral method; structured grid method; Cartesian grid method; immersed interface method; FFT; fast Poisson solver; geometric multigrid solver; GMRES iteration

*This work was supported in part by NIH grant R01HL76767.

Corresponding author. ying@math.duke.edu (Wenjun Ying), ch@cel-mail.bme.duke.edu (Craig S. Henriquez). URLs:<http://www.math.duke.edu/~ying> (Wenjun Ying), <http://www.bme.duke.edu/faculty/henriquez/index.php> (Craig S. Henriquez).

Publisher's Disclaimer: This is a PDF file of an unedited manuscript that has been accepted for publication. As a service to our customers we are providing this early version of the manuscript. The manuscript will undergo copyediting, typesetting, and review of the resulting proof before it is published in its final citable form. Please note that during the production process errors may be discovered which could affect the content, and all legal disclaimers that apply to the journal pertain.

1 Introduction

The finite difference and finite element methods are two major and competing numerical methods for solving elliptic boundary value problems (BVPs) [1]. The finite difference method is popular for simple structured domains and its ability to make use of fast solvers for constant coefficient BVPs. The finite element method is well-known for its flexibility to work with unstructured grids for problems on complex domains. The grid generation process associated with finite element method, however, is generally more challenging, particularly when the domain boundary is moving or the equation coefficients are discontinuous. Consequently, some recent research interest has focused on the use of structured (Cartesian) grid methods, or meshfree methods [2–4], to avoid the problems with grid generation.

Most structured grid methods in the literature reformulate the BVP as an interface problem and work with finite difference method on Cartesian grids. The grid lines are not required to be aligned with the domain boundary or the interface of discontinuities, which generally degrades the accuracy of numerical solutions. To recover the original accuracy of the finite difference method, techniques such as smoothing or regularization of discontinuities or correction of the discretization scheme are usually employed.

Representative existing methods are the immersed boundary (IB) method originally developed by C. S. Peskin in the 1970s [5–7], the immersed interface (II) method proposed by R. J. LeVeque and Z. Li [8], the ghost of fluid (GF) method originally developed by S. Osher and his coworkers [9, 10] and later extended by X.-D. Liu [11, 12] and A. Mayo's grid-based boundary integral method [13, 14].

In the IB method, the complex domain boundary is regarded as being immersed in a fluid and modeled via a singular source on the interface. The IB method is a smoothing method with a transition region that smears discontinuities as it uses a discrete delta function to distribute the singular source to nearby grid nodes. It is typically only first-order accurate in higher space dimensions. Some high order IB schemes have been proposed recently in the literature ([15–21]).

Unlike the IB method, the II method is a sharp interface method. In the II method, the finite difference stencil used to discretize the interface problem is modified at irregular grid nodes, where the discrete elliptic operator makes use of nodes from both sides of the interface. This is achieved by incorporating interface jump conditions into local Taylor expansions of the elliptic operator at the irregular grid nodes. The resulting scheme is of second-order accuracy and preserves the jumps across the interface. Modern versions of the II method are robust and efficient [22–27], and has been successfully applied to a variety of interface-related problems [28–33].

The II method has also been generalized for discretization of a non-diagonal anisotropic Laplacian in both two and three space dimensions by M. Dumett and J. P. Keener [34, 35]. Their method is currently first-order only, but it is stable for a wide range of anisotropic matrices when the anisotropy ratio is not too large and not too small. The resulting matrix with the method is nonsymmetric nonnegative definite.

In the GF method, the boundary or interface jump conditions are captured implicitly by extending values across the interface into a ghost fluid. On irregular grid nodes, when the finite difference discretized Laplacian refers to a node from the other side of the interface, a ghost fluid value instead of the real one will be supplied. Such a jump condition capturing procedure is directly incorporated into the numerical discretization in a way that the symmetry of the finite difference coefficient matrix is maintained. The original GF method [11, 12] for the variable coefficient Poisson equation is first-order accurate only. A recent

work by S. Hou and X.-D. Liu [36] shows that the GF method has been further extended to work with triangular grids, resulting in a second-order accurate method.

Mayo's approach combines boundary integral equations with finite difference methods to solve Poisson and biharmonic equations on irregular domains [13, 14, 37–40]. The complex domain is embedded into a larger rectangular domain, and the problem is reformulated as an elliptic interface problem such that the solution is harmonic in the rectangle, excluding the boundary of the original domain. After the source density is solved from the boundary integral equation, the jumps of the solution and its partial derivatives are naturally calculated. To recover the formal accuracy of the underlying finite difference scheme, the jumps are further used to make corrections for the right hand side of the discrete linear system corresponding to the irregular grid nodes. The corrected linear system is finally solved using a fast Poisson solver. The grid-based boundary integral method has been generalized to different problems such as biharmonic equations, Stokes and Navier-Stokes equations. Recently, J. T. Beale proposed methods for evaluating the (nearly) singular integrals in both two and three space dimensions, which make the grid-based boundary integral method more accurate [41, 42]. Mayo's approach is fast when combined with the fast multipole method [43] provided that the Green's functions are analytically known.

Other Cartesian grid methods similar to the II and GF methods include Berthelsen's decomposed II method [44], Zhou etc.'s high order matched interface and boundary (MIB) method [45], Johansen and Colella's volume of fluid (VOF) method [46, 47], Tseng and Ferziger's ghost-cell immersed boundary method [48], Oevermann and Klein's Cartesian grid finite volume method [49]. More methods that use Cartesian grids are the phase field method by J. W. Cahn and J. E. Hilliard [50] and the capacitance matrix method by W. Proskurowski and O. Widlund [51].

This paper presents a class of kernel-free boundary integral (KFBI) methods for solving the elliptic BVPs. It is similar, in spirit, to Li's augmented strategy for constant coefficient problems [25], Wiegmann and Bube's explicit jump II method [26] and Calhoun's Cartesian grid method [52], and is a direct extension of Mayo's original approach [13, 41, 42]. The most obvious difference of the method from others is that it works with more general elliptic operators with possible anisotropy and inhomogeneity. The KFBI method iteratively solves the boundary integral equations with a Krylov subspace method, the GMRES method [53,54]. During the iteration, the double/single layer potentials are approximated by limit values of structured grid-based numerical solutions while direct evaluation of the volume and boundary integrals is avoided. Hence, the analytical expressions of Green's functions are not required. The KFBI method assumes that the larger regular domain, into which the original complex domain is embedded, can be easily partitioned into a hierarchy of structured grids so that fast elliptic solvers such as the fast Fourier transform (FFT) based Poisson (Helmholtz) solvers or those based on geometric multigrid iterations are applicable. Because the irregular nodes on the structured grids introduce lower order errors, the method corrects the right hand side of the discrete linear system, based on the unknown density computed in the previous GMRES iteration step and the jump relations of the double or single layer potential and its flux, recovering the formal accuracy of the applied numerical scheme.

In section 2, we describe the inhomogeneous and anisotropic elliptic boundary value problems to be solved. In section 3, some results from the potential theory for the general elliptic BVPs are presented. In section 4, we give the boundary integral equations corresponding to the Dirichlet and Neumann BVPs and the iterations used to solve the boundary integral equations. The KFBI algorithm is summarized in section 5. In section 6, we show the interface problems for the computation of volume and boundary integrals.

Section 7 describes the spatial discretization of the interface problem on the larger regular domain with structured grids. Section 8 explains how to calculate jumps of the solution derivatives with the known densities. Section 9 derives the correction formula for the linear system resulting from spatial discretization of the interface on the structured grid. Section 10 gives the interpolation technique to extract values of the volume and boundary integrals at points on the boundary curve. Numerical results with the KFBI method for Dirichlet and Neumann BVPs are presented in section 11. Finally, the advantages, disadvantages and applications of the method are discussed in section 12.

2 Boundary Value Problems

The kernel-free boundary integral (KFBI) method described here is valid for general elliptic boundary value problems (BVPs) with either Dirichlet or Neumann boundary conditions on either simply or multiply connected bounded domains. For simplicity of explanation, we restrict ourselves to the discussion on the application of the method for solving BVPs on simply connected bounded domains. For the same reason, we only present the method in two space dimensions. Its extension to three space dimension is analogous.

Let $\Omega \subset \mathbb{R}^2$ be a simply connected bounded domain with smooth boundary $\partial\Omega$. Let \mathcal{B} be a larger regular domain, which completely contains the domain Ω . Assume that the boundaries of the original complex domain Ω and the regular domain \mathcal{B} have no intersection, i.e., $\Omega \subset \mathcal{B}$ and $\Omega \cap \mathcal{B} = \emptyset$. Denote by $\Omega^c \equiv \mathcal{B} \setminus \Omega$ the complement of the domain Ω in \mathcal{B} .

The regular domain \mathcal{B} can be chosen flexibly to be a triangle, a rectangle, a circle, a ring or any other regularly shaped domains as long as the Green's function on \mathcal{B} exists and fast elliptic solvers are readily available.

Let $\sigma \equiv \sigma(\mathbf{p})$ be a symmetric and positive definite (SPD) diffusion tensor and $k \equiv k(\mathbf{p})$ be a non-negative reaction coefficient. Assume that both are well defined in the regular domain \mathcal{B} . Then we introduce an (negative) elliptic operator

$$\mathcal{L} \equiv \nabla \cdot \sigma(\mathbf{x}) \nabla - \mathbf{k}(\mathbf{x}). \quad (1)$$

Additionally, assume that the diffusion tensor $\sigma(\mathbf{x})$ and the reaction coefficient $k(\mathbf{x})$ are at least continuously differentiable over the regular domain \mathcal{B} . In practice, these two quantities may only be defined inside the original complex domain Ω . In this case, we could use the KFBI method proposed here to derive biharmonic extensions of $\sigma(\mathbf{p})$ and $k(\mathbf{p})$ by solving biharmonic equations in the complement Ω^c such that the diffusion tensor, the reaction coefficient and their normal derivatives across the domain boundary are continuous.

Let $H^{r-1}(\Omega)$, $H^{r+1/2}(\Omega)$ and $H^{r-1/2}(\Omega)$ be the standard Sobolev spaces, with $r > k$ and k being a positive integer. Given a source function $f \in H^{r-1}(\Omega)$ and boundary data $g^D \in H^{r+1/2}(\Omega)$ or $g^N \in H^{r-1/2}(\Omega)$, we consider solving the elliptic equation

$$\mathcal{L}u(\mathbf{p}) = \mathbf{f}(\mathbf{p}) \text{ in } \Omega, \quad (2)$$

with either the pure Dirichlet boundary condition

$$u(\mathbf{p}) = g^D(\mathbf{p}) \text{ on } \partial\Omega, \quad (3)$$

or the pure Neumann boundary condition

$$\mathbf{n} \cdot \sigma \nabla u(\mathbf{p}) = \mathbf{g}^N(\mathbf{p}) \text{ on } \partial\Omega, \quad (4)$$

respectively. Here, \mathbf{n} denotes the unit outward normal pointing outside of the bounded domain Ω . The equations (2) and (3) form an *interior Dirichlet boundary value problem*. The equations (2) and (4) form an *interior Neumann boundary value problem*. Based on the assumptions described above, these two BVPs are well-posed (except that, when $k(\mathbf{x}) = 0$, the solution to the Neumann BVP is not unique but only up to an additive constant).

In this work, we assume that all of the variables and functions encountered are smooth enough such that the derivatives that appear are meaningful.

For a piecewise smooth dependent variable $v(\mathbf{p})$, defined on the larger regular domain \mathcal{B} , which has possible discontinuities only on the domain boundary Ω , let

$$v^+(\mathbf{p}) \equiv \lim_{\substack{q \in \Omega \\ q \rightarrow \mathbf{p}}} v(q) \text{ and } v^-(\mathbf{p}) \equiv \lim_{\substack{q \in \Omega^c \\ q \rightarrow \mathbf{p}}} v(q) \text{ for } \mathbf{p} \in \partial\Omega \quad (5)$$

be the limit values of $v(\mathbf{p})$ from either side of the domain boundary. Assume the domain Ω is on the positive side of the boundary curve Ω while the complementary domain Ω^c is on the negative side. The jump of the variable $v(\mathbf{p})$ across the domain boundary from negative to positive side is denoted by

$$[v(\mathbf{p})] \equiv v^+(\mathbf{p}) - v^-(\mathbf{p}) \text{ on } \partial\Omega. \quad (6)$$

3 Basics of Potential Theory

Let us first summarize some facts from the potential theory [55–59] for the general elliptic operator \mathcal{L} as it is the foundation of the KFBI method.

Let $G(\mathbf{q}; \mathbf{p})$ be the Green's function of the elliptic operator \mathcal{L} on the regular domain \mathcal{B} , which satisfies

$$\mathcal{L}G(\mathbf{q}; \mathbf{p}) = \delta(\mathbf{q} - \mathbf{p}) \text{ in } \mathcal{B}, \quad (7a)$$

$$G(\mathbf{q}; \mathbf{p}) = 0 \text{ on } \partial\mathcal{B}, \quad (7b)$$

for each fixed $\mathbf{p} \in \mathcal{B}$. Here, δ is the Dirac delta function.

Theorem 1

If the source function $f(\mathbf{p})$ in (2) is bounded and integrable in Ω , then the solution to the elliptic equation (2) with homogeneous Dirichlet boundary conditions, i.e., $g^D(\mathbf{p}) \equiv 0$, can be expressed as an integral of the product of the source function $f(\mathbf{p})$ and the Green's function $G(\mathbf{q}; \mathbf{p})$, i.e.,

$$u(\mathbf{p}) = (\mathcal{G}f)(\mathbf{p}) \equiv \int_{\Omega} \mathbf{G}(\mathbf{q}; \mathbf{p}) \mathbf{f}(\mathbf{q}) d\mathbf{q}. \quad (8)$$

Here, \mathcal{G} represents the volume integral operator. Moreover, the solution is continuously differentiable in \mathcal{B} if $f(\mathbf{p})$ is continuous in Ω .

Define two integral operators $\mathcal{K}: H^{1/2}(\Omega) \rightarrow H^{1/2}(\Omega)$ and $\mathcal{K}^*: H^{-1/2}(\Omega) \rightarrow H^{-1/2}(\Omega)$ by

$$(\mathcal{K}\varphi)(\mathbf{p}) \equiv \int_{\partial\Omega} \mathbf{n}_q \cdot \sigma(\mathbf{q}) \nabla \mathbf{G}(\mathbf{q}; \mathbf{p}) \varphi(\mathbf{q}) \mathbf{d}\mathbf{s}_q \text{ for } \varphi \in \mathbf{H}^{1/2}(\partial\Omega), \quad (9a)$$

$$(\mathcal{K}^*\psi)(\mathbf{p}) \equiv \int_{\partial\Omega} \mathbf{n}_p \cdot \sigma(\mathbf{p}) \nabla \mathbf{G}(\mathbf{q}; \mathbf{p}) \psi(\mathbf{q}) \mathbf{d}\mathbf{s}_q \text{ for } \psi \in \mathbf{H}^{-1/2}(\partial\Omega), \quad (9b)$$

with kernels

$$K(\mathbf{p}, \mathbf{q}) \equiv \mathbf{n}_q \cdot \sigma(\mathbf{q}) \nabla \mathbf{G}(\mathbf{q}; \mathbf{p}), \quad (10a)$$

$$K^*(\mathbf{p}, \mathbf{q}) \equiv \mathbf{n}_p \cdot \sigma(\mathbf{p}) \nabla \mathbf{G}(\mathbf{q}; \mathbf{p}), \quad (10b)$$

respectively.

Theorem 2

The boundary integral operator \mathcal{K} defined in (9a) introduces a double layer potential

$$u(\mathbf{p}) = (\mathcal{K}\varphi)(\mathbf{p}) \quad (11)$$

with density $\varphi(\mathbf{q}) \in H^{1/2}(\Omega)$. The double layer potential (11) has a jump across the domain boundary with strength equal to $\varphi(\mathbf{q})$ while the normal flux $\mathbf{n}_p \cdot \sigma \nabla u(\mathbf{p})$ is continuous. Specifically,

$$u^+(\mathbf{p}) - u(\mathbf{p}) = \frac{1}{2} \varphi(\mathbf{p}) \text{ on } \partial\Omega, \quad (12a)$$

$$u^-(\mathbf{p}) - u(\mathbf{p}) = -\frac{1}{2} \varphi(\mathbf{p}) \text{ on } \partial\Omega, \quad (12b)$$

and

$$\mathbf{n} \cdot \sigma \nabla u^+(\mathbf{p}) = \mathbf{n} \cdot \sigma \nabla u^-(\mathbf{p}) \text{ on } \partial\Omega \quad (13)$$

Theorem 3

Related to the boundary integral operator \mathcal{K}^* defined in (9b), a single layer potential is introduced by

$$u(\mathbf{p}) = -(\mathcal{N}\psi)(\mathbf{p}) \equiv -\int_{\partial\Omega} \mathbf{G}(\mathbf{q}; \mathbf{p}) \psi(\mathbf{q}) \mathbf{d}\mathbf{s}_q \quad (14)$$

with density $\psi(\mathbf{q}) \in H^{-1/2}(\Omega)$. The single layer potential (14) is continuous across the domain boundary Ω but the normal flux $\mathbf{n}_p \cdot \sigma \nabla u(\mathbf{p})$ has a jump with strength equal to $\psi(\mathbf{q})$. Specifically,

$$u^+(\mathbf{p}) = u^-(\mathbf{p}) \text{ on } \partial\Omega \quad (15)$$

and

$$\mathbf{n} \cdot \sigma \nabla u^+(\mathbf{p}) - \mathbf{n} \cdot \sigma \nabla u(\mathbf{p}) = \frac{1}{2} \psi(\mathbf{p}) \text{ on } \partial\Omega, \quad (16a)$$

$$\mathbf{n} \cdot \sigma \nabla u^-(\mathbf{p}) - \mathbf{n} \cdot \sigma \nabla u(\mathbf{p}) = -\frac{1}{2} \psi(\mathbf{p}) \text{ on } \partial\Omega. \quad (16b)$$

Theorem 4

In the regular domain \mathcal{B} excluding the domain boundary Ω , the double and single layer potentials satisfy the elliptic equation (2) with the source term $f(\mathbf{p})$ vanishing, i.e.,

$$\mathcal{L}(\mathcal{K}\varphi) = 0 \text{ in } \mathcal{B} \setminus \partial\Omega, \quad (17a)$$

$$\mathcal{L}(\mathcal{N}\psi) = 0 \text{ in } \mathcal{B} \setminus \partial\Omega. \quad (17b)$$

Finally, we have the following theorem on the spectrum of the integral operators (cf. Kellogg [55] or Kress [57] etc.).

Theorem 5

The integral operators defined in (9a) and (9b) are adjoint to each other. Both of them have the same spectrum, which is contained in the interval $(-1/2, 1/2]$. The constant $\lambda = 1/2$ can be an eigenvalue of the operators only if the reaction coefficient in the elliptic operator \mathcal{L} vanishes, i.e., $\kappa = 0$.

4 Boundary Integral Equations

The solution to the Dirichlet boundary value problem, defined by (2) and (3), can be expressed as a sum of a volume integral and a double layer potential

$$u(\mathbf{p}) = (\mathcal{G}\mathbf{f})(\mathbf{p}) + (\mathcal{K}\varphi)(\mathbf{p}) \text{ in } \Omega \quad (18)$$

with density $\varphi(\mathbf{p})$ satisfying the boundary integral equation

$$\frac{1}{2}\varphi + \mathcal{K}\varphi + \mathcal{G}\mathbf{f} = \{g^D \text{ on } \partial\Omega. \quad (19)$$

The solution to the Neumann boundary value problem, defined by (2) and (4), can be expressed as a sum of a volume integral and a single layer potential

$$u(\mathbf{p}) = (\mathcal{G}\mathbf{f})(\mathbf{p}) - (\mathcal{N}\psi)(\mathbf{p}) \text{ in } \Omega \quad (20)$$

with density $\psi(\mathbf{p})$ satisfying the boundary integral equation

$$\frac{1}{2}\psi - \mathcal{K}^*\psi + \mathbf{n} \cdot \sigma \nabla(\mathcal{G}\mathbf{f}) = \mathbf{g}^N \text{ on } \partial\Omega. \quad (21)$$

By the spectrum properties of the integral operators, both the integral equations, (19) and (21), are non-singular for general SPD diffusion tensor σ and reaction coefficient $k > 0$ except that, when the reaction coefficient is equal to zero ($\kappa = 0$), the integral equation (21) corresponding to the Neumann BVP becomes singular. In the non-singular cases, those two integral equations can be respectively solved by the following simple iterations:

$$u_v = \frac{1}{2}\varphi_v + \mathcal{K}\varphi_v + \mathcal{G}f, \quad (22a)$$

$$\varphi_{v+1} = \varphi_v + 2\beta(g^D - u_v) \quad (22b)$$

and

$$\mathbf{n}_p \cdot \sigma \nabla u_v = \frac{1}{2}\psi_v - \mathcal{K}^*\psi_v + \mathbf{n}_p \cdot \sigma \nabla(\mathcal{G}f), \quad (23a)$$

$$\psi_{v+1} = \psi_v + 2\beta(g^N - \mathbf{n}_p \cdot \sigma \nabla u_v) \quad (23b)$$

for $v = 0, 1, 2, \dots$, with iteration parameter $\beta \in (0, 1)$. Each of the simple iterative methods converges to a prescribed tolerance within a fixed number of steps with any initial guess φ_0 or ψ_0 in the solution space. The number of iterations depends on the shape of the domain, the diffusion tensor σ and the reaction coefficient k . For the singular integral equation corresponding to the Neumann BVP with vanishing reaction coefficient ($\kappa = 0$), an additional technique has to be applied for the simple iteration to converge.

For general elliptic operators, due to the un-availability of Green's functions, it is usually very difficult to directly evaluate the volume and boundary integrals in (22) and (23). For this, we only calculate them approximately. The analytical expressions of Green's functions are not required. In this sense, the method proposed in this work is called a *kernel-free boundary integral method*.

The densities, φ_v and ψ_v , are discretized by periodic cubic splines, which allow easy and efficient calculation of derivatives of the densities. Specifically, we assume that we are given M_Ω quasi-uniformly spaced nodes on the boundary Ω (see Fig. 1). Only at the curve nodes are the values of the density, φ or ψ , updated by the simple iterations (22) and (23). For the Dirichlet BVP, the right hand side of (22a) is replaced by the limit values of a grid-based approximate solution. For the Neumann BVP, the right hand side of (23a) is replaced by the limit values of the normal flux of an approximate solution. The details of the procedure for computing the limit values will be described in section 10.

As the right hand sides of (22a) and (23a) are approximated by grid-based numerical solutions, the maximum eigenvalues of the discrete boundary integral operators,

corresponding to \mathcal{K} and \mathcal{K}^* , could be larger than a half but each has an error to the exact one on the order of a power of the grid size that is used to derive the approximate solution [60–62]. From the viewpoint of practical implementation, the iteration parameter β will have an upper bound slightly less than one, and the simple iterations, (22) and (23), are still guaranteed to converge as long as the grids used to compute the approximate solutions are fine enough such that the maximum eigenvalues of the discrete integral operators are bounded by one, for example.

Nevertheless, the simple iterations for solving the boundary integral equations could be further improved by a Krylov subspace method such as the GMRES iteration [53,54]. For example, if we rewrite the boundary integral equation (19) as

$$\overline{\mathcal{K}}\varphi = \overline{g}^D \text{ on } \partial\Omega, \quad (24)$$

with

$$\overline{\mathcal{K}}\varphi \equiv \frac{1}{2}\varphi + \mathcal{K}\varphi, \overline{g}^D \equiv g^D - \mathcal{G}f, \quad (25)$$

and rewrite the boundary integral equation (21) as

$$\overline{\mathcal{K}}^*\psi = \overline{g}^N \text{ on } \partial\Omega, \quad (26)$$

with

$$\overline{\mathcal{K}}^*\psi \equiv \frac{1}{2}\psi - \mathcal{K}^*\psi, \overline{g}^N \equiv g^N - \mathbf{n} \cdot \sigma \nabla(\mathcal{G}\mathbf{f}), \quad (27)$$

the application of the GMRES iterative method to solving (24) and (26) simply requires computation of \overline{g}^D , \overline{g}^N and the actions $\mathcal{K}\varphi$, $\mathcal{K}^*\psi$ of the operators \mathcal{K} , \mathcal{K}^* on φ and ψ , respectively. Once again, the right hand sides of (25) and (27) can be approximated by limit values of approximate solutions to the Dirichlet BVP while direct evaluation of volume and boundary integrals are avoided.

5 Algorithm Overview

The key to the KFBI method for solving the boundary integral equation, (19) or (21), with the simple iterations described in section 4 or the GMRES method, is the approximation of the associated volume and boundary integrals using structured grid based solutions. The procedure for computing Gf and $N\varphi_v$ during each iteration is summarized as follows:

Step 1. *Set up the domain boundary. Partition the boundary curve into a set of quasi-uniformly spaced curve segments. Denote the discretization nodes by $\mathbf{q}_j (j = 1, 2, \dots, M_\Omega)$. Compute normals, tangents and curvatures of the boundary at the discretization nodes.*

Step 2. *Set up the structured grid. Embed the complex domain Ω into a larger regular domain \mathcal{Q} . Partition \mathcal{Q} into a hierarchy of structured grids. Denote the finest grid by \mathcal{T}_h . Identify regular and irregular nodes of the structured grid \mathcal{T}_h . Locate the points where the domain boundary Ω intersect with the edges (and diagonals) of the elements of grid \mathcal{T}_h . Compute tangential and normal unit directions of the boundary curve at those intersected points too.*

Step 3. Discretize the elliptic operator \mathcal{L} on the structured grid \mathcal{T}_h with the finite difference method or the finite element method. Denote the stiffness matrix by \mathbf{A}_h . Similarly, assemble the right hand side of the linear system, denoted by \mathbf{f}_h .

Step 4. Following section 8, given the approximate density ϕ_v or ψ_v , compute the jumps of the solution and its partial derivatives, $[u_v], [u_v/x], [u_v/y], [^2u_v/x^2], [^2u_v/x y]$ and $[^2u_v/y^2]$, at the points where the domain boundary intersect with the edges (and diagonals) of the elements of the grid \mathcal{T}_h .

Step 5. Following section 9, with the jumps computed in step 4, compute the correction formula $C_{v,h}$ and modify the right hand side \mathbf{f}_h . Denote the resulting source term by $\mathbf{f}_{v,h}$.

Step 6. Solve the modified linear system $\mathbf{A}_h \mathbf{u}_{v,h} = \mathbf{f}_{v,h}$ with a fast elliptic solver such as the FFT-based Poisson (Helmholtz) solver or a geometric multigrid solver.

Step 7. Following section 8, with the approximate density ϕ_v or ψ_v , compute the jumps of the solution and its partial derivatives, $[u_{v,h}], [u_{v,h}/x], [u_{v,h}/y], [^2u_{v,h}/x^2], [^2u_{v,h}/x y]$ and $[^2u_{v,h}/y^2]$, at the discretization nodes of the boundary curve, $\mathbf{q}_j (j= 1, 2, \dots, M_\Omega)$.

Step 8. Following section 10, use the jumps computed in step 7 to compute the limiting values of the approximate solution $u_{v,h}$ or its normal flux $\mathbf{n} \cdot \sigma \nabla u_{v,h}$ at the curve nodes $\mathbf{q}_j (j= 1, 2, \dots, M_\Omega)$.

Note that the steps 1-3 above need to be executed only once. The limiting values computed in step 8 will approximate the volume or boundary integrals ($Gf, K\phi_v, N\psi_v$ or $\kappa^* \psi_v$), respectively. With the approximation, the unknown density ϕ_v or ψ_v is updated by the simple iterations described in section 6, or the GMRES iterative method [53,54]. Then repeating steps 4-8 above continues the iteration until a stopping criterion is met (say, the residual is small enough).

In the limit as the iteration for the density ϕ_v or ψ_v converges, the grid-based numerical solution $u_{v,h}$ is naturally an accurate approximation of the exact one.

6 Computation of the Volume and Boundary Integrals

Following Mayo's approach [37], the volume integral $v = \mathcal{G}f$ occurring in the boundary integral equations above is computed by solving the following interface problem with discontinuous inhomogeneous source

$$\mathcal{L}v(\mathbf{p}) = \tilde{\mathbf{f}}(\mathbf{p}) \equiv \begin{cases} f(\mathbf{p}) & \text{in } \Omega \\ 0 & \text{in } \Omega^c \end{cases}, \quad (28a)$$

$$v^+(\mathbf{p}) = v^-(\mathbf{p}) \text{ on } \partial\Omega, \quad (28b)$$

$$\mathbf{n} \cdot \sigma \nabla v^+(\mathbf{p}) = \mathbf{n} \cdot \sigma \nabla v^-(\mathbf{p}) \text{ on } \partial\Omega, \quad (28c)$$

$$v(\mathbf{p}) = \mathbf{0} \text{ on } \partial\mathcal{B}. \quad (28d)$$

The double layer potential/integral $v = \kappa \phi$ is computed by solving an interface problem,

$$\mathcal{L}v(\mathbf{p})=\mathbf{0} \text{ in } \mathcal{B}\setminus\partial\Omega, \quad (29a)$$

$$v^+(\mathbf{p})=v^-(\mathbf{p})+\varphi(\mathbf{p}) \text{ on } \partial\Omega, \quad (29b)$$

$$\mathbf{n} \cdot \sigma \nabla v^+(\mathbf{p})=\mathbf{n} \cdot \sigma \nabla v^-(\mathbf{p}) \text{ on } \partial\Omega, \quad (29c)$$

$$v(\mathbf{p})=\mathbf{0} \text{ on } \partial\mathcal{B}. \quad (29d)$$

The single layer potential/integral $v = -\mathcal{N}\psi$ is computed by solving another similar interface problem,

$$\mathcal{L}v(\mathbf{p})=0 \text{ in } \mathcal{B}\setminus\partial\Omega, \quad (30a)$$

$$v^+(\mathbf{p})=v^-(\mathbf{p}) \text{ on } \partial\Omega, \quad (30b)$$

$$\mathbf{n} \cdot \sigma \nabla v^+(\mathbf{p})=\mathbf{n} \cdot \sigma \nabla v^-(\mathbf{p})+\psi(\mathbf{p}) \text{ on } \partial\Omega, \quad (30c)$$

$$v(\mathbf{p})=\mathbf{0} \text{ on } \partial\mathcal{B}. \quad (30d)$$

The boundary integral $\mathcal{K}^*\psi$ on the domain boundary Ω is by definition computed as the normal flux of the single layer potential/integral, i.e.,

$$\mathcal{K}^*\psi=\mathbf{n} \cdot \sigma \nabla(\mathcal{N}\psi). \quad (31)$$

Note that the three interface problems above, (28)-(30), can be presented and solved in a unified framework.

In the rest of this paper, for simplicity, we only illustrate the KFBI method for solving the Dirichlet boundary value problem. The extension of the method to solving the Neumann BVP is analogous.

As indicated by (18), the solution to the Dirichlet BVP described by Eqns. (2) and (3) is a sum of the solutions to the interface problems (28) and (29). In other words, the Dirichlet BVP is equivalent to the following interface problem:

$$\mathcal{L}u(\mathbf{p})=\tilde{\mathbf{f}}(\mathbf{p}) \text{ in } \mathcal{B}\setminus\partial\Omega, \quad (32a)$$

$$u^+(\mathbf{p})=\mathbf{u}^-(\mathbf{p})+\varphi(\mathbf{p}) \text{ on } \partial\Omega, \quad (32b)$$

$$\mathbf{n} \cdot \sigma \nabla u^+(\mathbf{p})=\mathbf{n} \cdot \sigma \nabla u^-(\mathbf{p}) \text{ on } \partial\Omega, \quad (32c)$$

$$u(\mathbf{p})=\mathbf{0} \text{ on } \partial\mathcal{B}, \quad (32d)$$

with $\varphi(\mathbf{p})$ the double layer potential density, defined by the boundary integral equation (19). Without confusion, we still use the same symbol $u(\mathbf{p})$ to denote the solution to the interface problem (32).

Suppose that an approximation to the double layer potential density $\varphi(\mathbf{p})$ is known as an intermediate result of the simple iteration (22) or the GMRES iteration for the boundary integral equation (19) or (24). Denote the approximate density by $\varphi_v \equiv \varphi_v(\mathbf{p})$.

Given this density function φ_v in place of φ in (32b), the interface problem (32) is approximated by

$$\mathcal{L}u_v(\mathbf{p}) = \tilde{\mathbf{f}}(\mathbf{p}) \text{ in } \mathcal{B} \setminus \partial\Omega, \quad (33a)$$

$$u_v^+(\mathbf{p}) = u_v^-(\mathbf{p}) + \varphi_v(\mathbf{p}) \text{ on } \partial\Omega, \quad (33b)$$

$$\mathbf{n} \cdot \sigma \nabla u_v^+(\mathbf{p}) = \mathbf{n} \cdot \sigma \nabla u_v^-(\mathbf{p}) \text{ on } \partial\Omega, \quad (33c)$$

$$u_v(\mathbf{p}) = \mathbf{0} \text{ on } \partial\mathcal{B}, \quad (33d)$$

with $u_v \equiv u_v(\mathbf{p})$ being an approximation of $u(\mathbf{p})$, the solution of (32).

7 Spatial Discretization on Structured Grids

To further solve the interface problem (33) numerically, assume that the regular domain \mathcal{B} is partitioned into a uniform structured grid. Assume the grid has N interior nodes $\{\mathbf{p}_i\}_{i=1}^N$. Denote the mesh parameter of the grid by h .

On the uniform structured grid, the elliptic operator \mathcal{L} can be discretized with a standard grid-based method, such as the finite difference method, the finite element method or the finite volume method. Assume a k^{th} -order ($\kappa > 1$) scheme is used to discretize the elliptic operator \mathcal{L} . Denote the discrete elliptic operator by \mathcal{L}_h .

If the discretization scheme is the finite difference method, the discrete elliptic operator \mathcal{L}_h is explicitly available. For example, when the standard five-point stencil is used, the discrete elliptic operator \mathcal{L}_h has the form $\mathcal{L}_h = \mathbf{A}_h/h^2$, where the finite difference stiffness matrix \mathbf{A}_h is block tridiagonal with the natural ordering of grid nodes and the non-zero entries of \mathbf{A}_h are either 4 or -1 . Typically the following approximation property holds

$$|\mathcal{L}v - \mathcal{L}_h v|_\infty \equiv \max_{1 \leq i \leq N} |\mathcal{L}v(\mathbf{p}_i) - \mathcal{L}_h v(\mathbf{p}_i)| = O(h^k) \quad (34)$$

in the discrete maximum norm for v sufficiently smooth. However, if the discretization scheme is the finite element method or the finite volume method, the expression for the discrete elliptic operator \mathcal{L}_h may not be explicitly available. In this case, we assume the Dirichlet BVP:

$$\mathcal{L}w = \mathbf{f}^* \text{ in } \mathcal{B}, \quad (35a)$$

$$w=0 \text{ on } \partial\mathcal{B}, \quad (35b)$$

with $f^* \in H^{r-1}(\mathcal{B})$ ($r > k > 1$), is discretized by a k^{th} -order ($\kappa > 1$) finite element or finite volume method into the linear system

$$\mathbf{A}_h \mathbf{w}_h = \mathbf{M}_h \mathbf{f}^*. \quad (36)$$

Here, $\mathbf{A}_h \equiv (a_{i,j})_{N \times N}$ is the finite element stiffness matrix; $\mathbf{M}_h \equiv (m_{i,j})_{N \times N}$ is the mass matrix and each entry of the vector \mathbf{f}^* equals the value of the source f^* at the corresponding grid node, i.e.,

$$(f^*)_i \equiv f^*(\mathbf{p}_i) = (\mathcal{L}w)(\mathbf{p}_i) \text{ for } i=1, 2, \dots, N. \quad (37)$$

Let $\mathbf{v}_h \equiv (v(\mathbf{p}_1), v(\mathbf{p}_2), \dots, v(\mathbf{p}_N))^T$ be the vector with its i^{th} entry equal to the value of $v \in H_0^{r+1}(\mathcal{B})$ at the i^{th} grid node \mathbf{p}_i . For simplicity, we assume, with the uniform grid, there exists an invertible diagonal matrix $\mathbf{D}_h \equiv \text{diag}(d_i)_N$ such that

$$\max_{1 \leq i \leq N} |\mathcal{L}v(\mathbf{p}_i) - (\mathbf{D}_h^{-1} \mathbf{A}_h \mathbf{v})_i| = \mathbf{O}(h^k) \quad (38)$$

for any $v \in H_0^{r+1}(\mathcal{B})$ in the discrete maximum norm.

Introducing the notation:

$$\mathbf{D}_h^{-1} \mathbf{A}_h v(\mathbf{p}_i) \equiv (\mathbf{D}_h^{-1} \mathbf{A}_h \mathbf{v}_h)_i \text{ for } i=1, 2, \dots, N, \quad (39)$$

we could define the discrete elliptic operator \mathcal{L}_h by

$$\mathcal{L}_h v(\mathbf{p}_i) \equiv \mathbf{D}_h^{-1} \mathbf{A}_h v(\mathbf{p}_i) \text{ at grid node } \mathbf{p}_i, i=1, 2, \dots, N, \quad (40)$$

for $v \in H_0^{r+1}(\mathcal{B})$. Here, the coefficient matrix in the right hand side of (40) is understood as an operator of grid functions. Note that the assumption (38) indicates the approximation property of the discrete elliptic operator:

$$|\mathcal{L}v - \mathcal{L}_h v|_\infty \equiv \max_{1 \leq i \leq N} |\mathcal{L}v(\mathbf{p}_i) - \mathcal{L}_h v(\mathbf{p}_i)| = \mathbf{O}(h^k) \quad (41)$$

in the discrete maximum norm for $v \in H_0^{r+1}(\mathcal{B})$.

In general, the stiffness matrix $\mathbf{A}_h = (a_{i,j})_{N \times N}$ is sparse, symmetric and negative definite. Each row in the matrix \mathbf{A}_h corresponds to an interior node on the grid. For the i^{th} row in the matrix, which corresponds to the i^{th} grid node \mathbf{p}_i , we call the set of grid nodes

$$S(i) \equiv \{\mathbf{p}_j | a_{i,j} \neq 0\} \quad (42)$$

as the *discretization stencil* of the discrete elliptic operator \mathcal{L}_h at the grid node \mathbf{p}_i and the corresponding index set is denoted by

$$\mathcal{S}(i) \equiv \{j|a_{i,j} \neq 0\}. \quad (43)$$

A grid node \mathbf{p}_i is called *irregular* if there is a grid node $\mathbf{p}_j \in \mathcal{S}(i)$ such that the line segment $\overline{\mathbf{p}_j\mathbf{p}_i}$ connecting \mathbf{p}_j with \mathbf{p}_i intersects with the domain boundary Ω . Note the line segment $\overline{\mathbf{p}_j\mathbf{p}_i}$ may intersect with the boundary curve several times (see Fig. 2). Otherwise, the grid node \mathbf{p}_i is called *regular*. By the definition, a grid node may be irregular even though all of the nodes in its discretization stencil are on the same side of the boundary (see Fig. 2).

Suppose that the linear system resulting from discretizing the interface problem (33) with the k^{th} -order discretization scheme is given by

$$\mathcal{L}_h \tilde{u}_{v,h}(\mathbf{p}_i) = \tilde{f}(\mathbf{p}_i) \text{ at grid nodes } \mathbf{p}_i, i=1, 2, \dots, N. \quad (44)$$

In principle, the discretization scheme for the interface problem (33) should essentially have k^{th} -order accuracy if the jumps across the domain boundary of the solution $u_{\&nu}$ the flux $\mathbf{n} \cdot \sigma \nabla u_{\&nu}$, the extended source term \tilde{f} all vanish and additionally \tilde{f} is sufficiently smooth. However, the presence of discontinuities of the solution and the extended source term significantly degrade the accuracy of the solution $\tilde{u}_{v,h}$ to the linear system (44) since

$$|\mathcal{L}u_v(\mathbf{p}_i) - \mathcal{L}_h u_v(\mathbf{p}_i)| > O(h^k) \quad (45)$$

at irregular grid nodes \mathbf{p}_i . To recover the formal accuracy of the discretization scheme, the right hand side of the linear system (44), which approximates the extended source term $\tilde{f}(\mathbf{p})$, must be modified at irregular grid nodes.

Section 9 describes a correction formula $C_{v,h}(\mathbf{p})$ for the source term in (44). The correction is made such that

$$\mathcal{L}_h u_v(\mathbf{p}_i) - \mathcal{L}u_v(\mathbf{p}_i) = C_{v,h}(\mathbf{p}_i) + O(h^{k-1}), \quad (46)$$

at irregular grid nodes \mathbf{p}_i . Define the corrected source term as a grid function by

$$\tilde{f}_{v,h}(\mathbf{p}_i) \equiv \begin{cases} f(\mathbf{p}_i) & \text{if } \mathbf{p}_i \text{ is a regular point in } \Omega \\ f(\mathbf{p}_i) + C_{v,h}(\mathbf{p}_i) & \text{if } \mathbf{p}_i \text{ is an irregular point in } \Omega \\ C_{v,h}(\mathbf{p}_i) & \text{if } \mathbf{p}_i \text{ is an irregular point in } \Omega^c \\ 0 & \text{if } \mathbf{p}_i \text{ is a regular point in } \Omega^c \end{cases}, \quad (47)$$

for $i = 1, 2, \dots, N$. Finally, we obtain the following corrected linear system

$$\mathcal{L}_h u_{v,h}(\mathbf{p}_i) = \tilde{f}_{v,h}(\mathbf{p}_i) \text{ at grid nodes } \mathbf{p}_i, i=1, 2, \dots, N. \quad (48)$$

or the symmetric and negative definite one

$$\mathbf{A}_h u_{v,h}(\mathbf{p}_i) = \mathbf{D}_h \tilde{f}_{v,h}(\mathbf{p}_i) \text{ at grid nodes } \mathbf{p}_i, i=1, 2, \dots, N. \quad (49)$$

Like (39), each side of (49) is understood as the i^{th} entry of the corresponding matrix-vector product, or the matrices \mathbf{A}_h and \mathbf{D}_h are treated as operators of grid functions. The diagonal

matrix \mathbf{D}_h is replaced by the identity matrix \mathbf{I}_h if the discretization is based on the finite difference method.

As the stiffness matrix \mathbf{A}_h is symmetric and negative definite and a hierarchy of structured grids exist based upon the assumption on the regular domain \mathcal{B} , the system (49) can be efficiently solved with standard geometric multigrid iterations. In the case that the regular domain \mathcal{B} is a rectangle and the elliptic operator is homogeneous and isotropic, it may even be solved with the fast Fourier transform (FFT) based fast Poisson (Helmholtz) solvers.

8 Calculation of Jumps of the Partial Derivatives

Suppose that the domain boundary Ω is smooth enough (at least twice continuously differentiable). Let $\mathbf{t}(s) \equiv (\dot{x}(s), \dot{y}(s))^T$ be the unit tangential vector along the boundary. Here, s is the arc-length parameter. The outward normal \mathbf{n} is given by $\mathbf{n}(s) = (\dot{y}(s), -\dot{x}(s))^T$.

We present the calculation of jumps across Ω of the derivatives of the solution ($u \equiv u(\mathbf{p})$) to the Dirichlet or Neumann BVP in a unified framework. Assume that

$$\mathcal{L}u(\mathbf{p}) = \tilde{\mathbf{f}}(\mathbf{p}) \text{ in } \mathcal{B}, \quad (50a)$$

$$[u] = \varphi \text{ on } \partial\Omega, \quad (50b)$$

$$[\mathbf{n} \cdot \sigma \nabla u] = \psi \text{ on } \partial\Omega, \quad (50c)$$

$$u(\mathbf{p}) = \mathbf{0} \text{ on } \partial\mathcal{B}. \quad (50d)$$

For the Dirichlet BVP, the flux of the double layer potential is continuous across Ω , i.e., $\psi = 0$. For the Neumann BVP, the single layer potential is continuous across Ω , i.e., $\varphi = 0$.

Assume the (symmetric) diffusion tensor σ in \mathcal{L} has the form

$$\sigma = \begin{pmatrix} \sigma_{11} & \sigma_{12} \\ \sigma_{12} & \sigma_{22} \end{pmatrix}. \quad (51)$$

Writing out the jump (50c) of the normal flux $\mathbf{n} \cdot \sigma \nabla u$ gives us

$$(\dot{y}\sigma_{11} - \dot{x}\sigma_{12})[u_x] + (\dot{y}\sigma_{12} - \dot{x}\sigma_{22})[u_y] = \psi. \quad (52)$$

Differentiating (50b) in the tangential direction \mathbf{t} , we see that

$$[u_t] = \dot{x}[u_x] + \dot{y}[u_y] = \varphi_t. \quad (53)$$

The determinant of the two by two system (52)-(53) is equal to

$$D_2 \equiv \sigma_{11}\dot{y}^2 + \sigma_{22}\dot{x}^2 - 2\sigma_{12}\dot{x}\dot{y} = (\dot{y} - \dot{x})^T \begin{pmatrix} \sigma_{11} & \sigma_{12} \\ \sigma_{12} & \sigma_{22} \end{pmatrix} \begin{pmatrix} \dot{y} \\ -\dot{x} \end{pmatrix}, \quad (54)$$

which is always positive, uniformly bounded by a positive constant from below. So, the jumps $[u_x]$ and $[u_y]$ of the first-order derivatives can be solved from (52)-(53).

To compute the jumps ($[u_{xx}]$, $[u_{xy}]$ and $[u_{yy}]$) of the second-order derivatives of u , we differentiate (52) and (53) in the tangential direction and obtain

$$(\dot{y}\sigma_{11} - \dot{x}\sigma_{12})\dot{x}[u_{xx}] + (\dot{y}^2\sigma_{11} - \dot{x}^2\sigma_{22})[u_{xy}] + (\dot{y}\sigma_{12} - \dot{x}\sigma_{22})\dot{y}[u_{yy}] = r_0, \quad (55a)$$

$$\dot{x}^2[u_{xx}] + 2\dot{x}\dot{y}[u_{xy}] + \dot{y}^2[u_{yy}] = r_1, \quad (55b)$$

with

$$r_0 \equiv \psi_t - \frac{d(\dot{y}\sigma_{11} - \dot{x}\sigma_{12})}{ds}[u_x] - \frac{d(\dot{y}\sigma_{12} - \dot{x}\sigma_{22})}{ds}[u_y],$$

$$r_1 \equiv \varphi_{tt}(x) - \ddot{x}[u_x] - \ddot{y}[u_y].$$

In addition, denote by ρ the jump of the extended source \tilde{f} in (50a), i.e.,

$$[\mathcal{L}u] = \rho \text{ on } \partial\Omega. \quad (57)$$

Writing out (57) explicitly gives us

$$\sigma_{11}[u_{xx}] + 2\sigma_{12}[u_{xy}] + \sigma_{22}[u_{yy}] = r_2, \quad (58)$$

with

$$r_2 \equiv \rho + k[u] - (\sigma_{11,x} + \sigma_{12,y})[u_x] - (\sigma_{12,x} + \sigma_{22,y})[u_y].$$

The determinant of the coefficient matrix in the three by three system (55)-(57) is equal to

$$D_3 \equiv D_2^2 = (\sigma_{11}\dot{y}^2 + \sigma_{22}\dot{x}^2 - 2\sigma_{12}\dot{x}\dot{y})^2, \quad (59)$$

which is uniformly bounded by a positive constant from below too. So, the jumps ($[u_{xx}]$, $[u_{xy}]$ and $[u_{yy}]$) of the second-order derivatives of u can be uniquely solved from the three by three system (55)-(57).

We could similarly evaluate discontinuities in the third-order derivatives of $u(\mathbf{p})$. There are four such derivatives, $[u_{xxx}]$, $[u_{yyy}]$, $[u_{xxy}]$ and $[u_{xyy}]$. To determine the discontinuities in these derivatives we differentiate Eqns. (55) in the tangential direction \mathbf{t} and differentiate (57) in both the normal and tangential directions. This method can be used to compute discontinuities in higher order derivatives.

For the solution u_ν to the approximate interface problem (33), the jumps of its derivatives,

$$\left[\frac{\partial u_v}{\partial x} \right], \left[\frac{\partial u_v}{\partial y} \right], \left[\frac{\partial^2 u_v}{\partial x^2} \right], \left[\frac{\partial^2 u_v}{\partial x \partial y} \right] \text{ and } \left[\frac{\partial^2 u_v}{\partial y^2} \right], \quad (60)$$

can be calculated exactly in the same way as above.

9 Derivation of the Correction Formula

We focus on the correction of the linear systems discretized by the standard continuous second-order ($\kappa = 2$) finite element method since it can easily handle Dirichlet and Neumann boundary conditions associated with the general (possibly anisotropic) elliptic operator \mathcal{L} . Computation of the correction formula for those resulting from discretization with finite difference or finite volume method is similar.

With the continuous piecewise linear (or bilinear) finite elements, the diagonal matrix \mathbf{D}_h in (38) is obtained through the technique of mass lumping [63–67] for the mass matrix \mathbf{M}_h on the right hand side of the finite element system (36). The assumption (38) results from the numerical integration with grid nodes being the quadrature points.

As indicated by (46), the correction to the right hand side of the system (44) at irregular grid nodes \mathbf{p}_i is computed such that

$$\begin{aligned} C_{v,h}(\mathbf{p}_i) &= \mathcal{L}_h u_v(\mathbf{p}_i) - \mathcal{L} u_v(\mathbf{p}_i) + O(h) \\ &= \mathbf{D}_h^{-1} \mathbf{A}_h u_v(\mathbf{p}_i) - \mathcal{L} u_v(\mathbf{p}_i) + O(h) \\ &= \frac{1}{d_i} \sum_{j \in \mathcal{J}(i)} a_{i,j} u_v(\mathbf{p}_j) - \mathcal{L} u_v(\mathbf{p}_i) + O(h). \end{aligned} \quad (61)$$

First, for each grid node \mathbf{p}_i we define the truncated Taylor expansion of $u_v(\mathbf{p})$ around \mathbf{p}_i by

$$U_{v,i}(\mathbf{p}) \equiv \sum_{n=0}^2 \frac{\mathbf{1}}{n!} \frac{\partial^n \mathbf{u}_v(\mathbf{p}_i)}{\partial z^n} |\mathbf{p} - \mathbf{p}_i|^n + \mathbf{O}(|\mathbf{p} - \mathbf{p}_i|^3) \quad (62)$$

with the unit direction

$$\mathbf{z} \equiv \frac{\mathbf{p} - \mathbf{p}_i}{|\mathbf{p} - \mathbf{p}_i|} \quad (63)$$

for $\mathbf{p} \neq \mathbf{p}_i$. By the approximation property (41), we have

$$\mathcal{L} u_v(\mathbf{p}_i) - \frac{1}{d_i} \sum_{j \in \mathcal{J}(i)} a_{i,j} U_{v,i}(\mathbf{p}_j) = \mathcal{L} U_{v,i}(\mathbf{p}_i) - \frac{1}{d_i} \sum_{j \in \mathcal{J}(i)} a_{i,j} U_{v,i}(\mathbf{p}_j) = O(h^2). \quad (64)$$

By replacing $\mathcal{L} u_v(\mathbf{p}_i)$ in (61) with the weighted sum of the values of the truncated Taylor expansion $U_{v,i}(\mathbf{p})$ at grid nodes in the stencil, we could compute the correction formula using

$$C_{v,h} = \frac{1}{d_i} \sum_{j \in \mathcal{J}(i)} a_{i,j} (u_v(\mathbf{p}_j) - U_{v,i}(\mathbf{p}_j)) + O(h). \quad (65)$$

Notice that, with the second-order finite element method, the entries d_i of the diagonal matrix \mathbf{D}_h are on the order of h^2 . It is necessary and sufficient to compute the difference $u_v(\mathbf{p}_j) - U_{v,i}(\mathbf{p}_j)$ in (65) up to the third-order accuracy.

In the case that the line segment connecting the grid nodes \mathbf{p}_i and \mathbf{p}_j does not come across the domain boundary Ω , the difference between $u_v(\mathbf{p}_j)$ and $U_{v,i}(\mathbf{p}_j)$ has already been on the order of h^3 . In the correction formula (65), it is simply replaced by zero.

In the case that the line segment $\overline{\mathbf{p}_i\mathbf{p}_j}$ intersects with the domain boundary only once at a point \mathbf{q} (see Fig. 3(a)), if the node \mathbf{p}_i is in the complementary domain Ω^c and the node \mathbf{p}_j is in the interior of the domain Ω , the difference between $u_v(\mathbf{p}_j)$ and $U_{v,i}(\mathbf{p}_j)$ is computed as the difference of their Taylor expansions around \mathbf{q} , i.e.,

$$\begin{aligned} u_v(\mathbf{p}_j) - U_{v,i}(\mathbf{p}_j) &= \sum_{n=0}^2 \frac{1}{n!} \left(\frac{\partial^n u_v^+(\mathbf{q})}{\partial z^n} - \frac{\partial^n U_{v,i}(\mathbf{q})}{\partial z^n} \right) |\mathbf{p}_j - \mathbf{q}|^n + \mathbf{O}(h^3) \\ &= \sum_{n=0}^2 \frac{1}{n!} \left(\frac{\partial^n u_v(\mathbf{q})}{\partial z^n} \right) |\mathbf{p}_j - \mathbf{q}|^n + \mathbf{O}(h^3); \end{aligned} \tag{66}$$

if the node \mathbf{p}_i is in the interior of the domain Ω and the node \mathbf{p}_j is in the complementary domain Ω^c , the difference is computed by

$$\begin{aligned} u_v(\mathbf{p}_j) - U_{v,i}(\mathbf{p}_j) &= \sum_{n=0}^2 \frac{1}{n!} \left(\frac{\partial^n u_v^-(\mathbf{q})}{\partial z^n} - \frac{\partial^n U_{v,i}(\mathbf{q})}{\partial z^n} \right) |\mathbf{p}_j - \mathbf{q}|^n + \mathbf{O}(h^3) \\ &= - \sum_{n=0}^2 \frac{1}{n!} \left(\frac{\partial^n u_v(\mathbf{q})}{\partial z^n} \right) |\mathbf{p}_j - \mathbf{q}|^n + \mathbf{O}(h^3). \end{aligned} \tag{67}$$

When the line segment $\overline{\mathbf{p}_i\mathbf{p}_j}$ intersects with the domain boundary several times, the difference $u_v(\mathbf{p}_j) - U_{v,i}(\mathbf{p}_j)$ can be similarly computed but the procedure is more complicated because a multiplicative manipulation of the jumps will be involved each time when the line segment $\overline{\mathbf{p}_i\mathbf{p}_j}$ comes across the domain boundary Ω . Here, we only give the formula corresponding to the cases when the number of intersected points is two (see Fig. 3(b)): if both of the endpoints of the line segment $\overline{\mathbf{p}_i\mathbf{p}_j}$ are in the interior of the domain Ω ,

$$u_v(\mathbf{p}_j) - U_{v,i}(\mathbf{p}_j) = - \sum_{n=0}^2 \left\{ \sum_{m=0}^{2-n} \frac{1}{n!m!} \left[\frac{\partial^{n+m} u_v(\mathbf{q})}{\partial z^{n+m}} \right] |q_1 - q_2|^m \right\} |\mathbf{p}_j - \mathbf{q}_1|^n + \sum_{n=0}^2 \frac{1}{n!} \left[\frac{\partial^n u_v(\mathbf{q})}{\partial z^n} \right] |\mathbf{p}_j - \mathbf{q}_1|^n + \mathbf{O}(h^3); \tag{68}$$

if both of the endpoints are in the exterior of the domain Ω ,

$$u_v(\mathbf{p}_j) - U_{v,i}(\mathbf{p}_j) = \sum_{n=0}^2 \left\{ \sum_{m=0}^{2-n} \frac{1}{n!m!} \left[\frac{\partial^{n+m} u_v(\mathbf{q})}{\partial z^{n+m}} \right] |q_1 - q_2|^m \right\} |\mathbf{p}_j - \mathbf{q}_1|^n - \sum_{n=0}^2 \frac{1}{n!} \left[\frac{\partial^n u_v(\mathbf{q})}{\partial z^n} \right] |\mathbf{p}_j - \mathbf{q}_1|^n + \mathbf{O}(h^3). \tag{69}$$

Finally, the jumps of the directional derivatives ($n = 1, 2$),

$$\left[\frac{\partial^n u_v(\mathbf{q})}{\partial z^n} \right],$$

are calculated in terms of the known jumps of partial derivatives,

$$\left[\frac{\partial u_v(\mathbf{q})}{\partial x} \right], \left[\frac{\partial u_v(\mathbf{q})}{\partial y} \right], \quad (70)$$

and

$$\left[\frac{\partial^2 u_v(\mathbf{q})}{\partial x^2} \right], \left[\frac{\partial^2 u_v(\mathbf{q})}{\partial x \partial y} \right], \left[\frac{\partial^2 u_v(\mathbf{q})}{\partial y^2} \right]. \quad (71)$$

For piecewise constant coefficient elliptic equations, recently Beale and Layton [68] proved that, with the correction formula computed as above for the standard five-point finite difference scheme, the solution to the corrected linear system (49) is second-order accurate in the discrete maximum norm,

$$|u_{v,h} - u_v|_\infty = O(h^2). \quad (72)$$

For the general elliptic operator \mathcal{L} with possible anisotropy and inhomogeneity, a factor of $\log h$ will enter into the pointwise error estimate, which is stated in the following theorem.

Theorem 6

Assume that the number of irregular grid nodes is on the order of hN . The numerical solution $u_{v,h}$ to the corrected linear system (49) for the general elliptic BVP is essentially second-order in accuracy, i.e.,

$$|u_{v,h} - u_v|_\infty \equiv \max_{1 \leq i \leq N} |u_{v,h}(p_i) - u_v(p_i)| = O(h^2 |\log h|). \quad (73)$$

It can be shown that the pointwise error estimate (73) is true with either the finite difference method or the finite element method. In the next, we only prove it for the finite element method case.

We first need to introduce two lemmas related to discrete Green's functions. Let $S_h \subset H_0^1(\mathcal{B})$ be the standard finite element space consisting of continuous functions that are linear (bilinear) on each of the elements of \mathcal{T}_h and vanish outside \mathcal{T}_h . For a fixed grid node \mathbf{p}_i let \mathbf{c}_{ji} be a point in the interior of an element, which is adjacent to \mathbf{p}_i . Define a discrete Green's function g_{ji} by

$$(A_h g_{ji}, \chi) = \chi(\mathbf{c}_{ji}) \forall \chi \in S_h. \quad (74)$$

The partial derivatives $g_{ji,x}$ and $g_{ji,y}$ in the distributional sense of the discrete Green's function g_{ji} satisfy:

$$(A_h g_{ji,x}, \chi) = \frac{\partial \chi(\mathbf{c}_{ji})}{\partial x} \forall \chi \in S_h, \quad (75)$$

and

$$(A_h g_{j_i,y}, \chi) = \frac{\partial \chi(c_{j_i})}{\partial y} \forall \chi \in S_h, \quad (76)$$

respectively.

Lemma 7

$$\|g_{j_i,x}\|_{L^2} \leq C|\log h|^{1/2} \text{ and } \|g_{j_i,y}\|_{L^2} \leq C|\log h|^{1/2}. \quad (77)$$

Proof. We will prove the inequalities by a duality argument. For arbitrarily chosen $\varphi \in L^2(\mathcal{B})$, let ψ be the solution of the following BVP

$$\mathcal{L}\psi = \varphi \text{ in } \mathcal{B}, \quad (78a)$$

$$\psi = 0 \text{ on } \mathcal{B}. \quad (78b)$$

We have

$$(g_{j_i,x}, \varphi) = (A_h g_{j_i,x}, \psi) = (A_h g_{j_i,x}, R_h \psi) = \frac{\partial R_h \psi}{\partial x}. \quad (79)$$

Here, $R_h: H^2 \rightarrow S_h$ is the elliptic projection. It is proved by Rannacher and Scott [69] first for the Laplacian operator and later extended for the general elliptic operators (refer to Brenner and Scott [70]) that R_h is bounded in the Sobolev space $W_0^{1,p}$, uniformly in p for $p > 2$.

$$|(g_{j_i,x}, \varphi)| \leq \|R_h \psi\|_{W_0^{1,\infty}} \leq Ch^{-2/p} \|R_h \psi\|_{W_0^{1,p}} \leq Ch^{-2/p} \|\psi\|_{W_0^{1,p}}. \quad (80)$$

Furthermore, the Sobolev inequality

$$\|v\|_{L^p} \leq C\sqrt{p}\|v\|_{H^1}, \quad p > 2 \quad (81)$$

and the elliptic regularity estimate

$$\|\psi\|_{W_0^{1,p}} \leq C\sqrt{p}\|\psi\|_{H^2} \leq C\sqrt{p}\|\varphi\|_{L^2}, \quad (82)$$

indicate

$$|(g_{j_i,x}, \varphi)| \leq Ch^{-2/p} \sqrt{p}\|\varphi\|_{L^2}. \quad (83)$$

Letting $p = |\log h|$, we obtain

$$|(g_{j_i,x}, \varphi)| \leq C|\log h|^{1/2}\|\varphi\|_{L^2} \forall \varphi \in L^2(\mathcal{B}), \quad (84)$$

and hence the first inequality in the lemma. The proof for the second inequality is similar.

The following lemma in the finite difference case is some form of the results by Bramble and Thomée [71]. Here, we prove that the maximum norm estimate for the discrete Green's function is also true with the finite element method.

Lemma 8

$$|g_{ji}|_{L^\infty} \leq C|\log h|. \quad (85)$$

Proof. By the Sobolev embedding inequality, for $p > 2$, $H^1(\mathcal{K}) \hookrightarrow L^p(\mathcal{K})$,

$$\|v\|_{L^p} \leq C\sqrt{p}\|v\|_{H^1}, \forall v \in S_h. \quad (86)$$

By the inverse estimate in the finite element space S_h ,

$$\|v\|_{L^\infty} \leq Ch^{-2/p}\|v\|_{L^p}. \quad (87)$$

So,

$$\|v\|_{L^\infty} \leq Ch^{-2/p}\sqrt{p}\|v\|_{H^1} \leq Ch^{-2/p}\sqrt{p}|v|_{H^1_0}. \quad (88)$$

Let $p = |\log h|$. We have

$$\|v\|_{L^\infty} \leq C|\log h|^{1/2} \left(\left\| \frac{\partial v}{\partial x} \right\|_{L^2} + \left\| \frac{\partial v}{\partial y} \right\|_{L^2} \right). \quad (89)$$

Finally, plugging $v = g_{ji}$ into (89), we obtain

$$|g_{ji}|_{L^\infty} \leq C|\log h|^{1/2} (\|g_{ji,x}\|_{L^2} + \|g_{ji,y}\|_{L^2}) \leq C|\log h|. \quad (90)$$

As $\mathbf{c}_{ji} \rightarrow \mathbf{p}_i$ in the limit of (85), we have

Lemma 9

$$|g_i|_{L^\infty} \leq C|\log h|, \quad (91)$$

for the discrete Green's function g_i given by

$$(A_h g_i, \chi) = \chi(\mathbf{p}_i) \forall \chi \in S_h. \quad (92)$$

Let g_i be the vector with its components equal to the nodal values of the discrete Green's function g_i in Lemma 9. Let $\mathbf{e}_j = (0, \dots, 0, 1, 0, \dots, 0)^T$ be the unit vector with only the j^{th} entry equal to one and all others vanishing. Then the vector \mathbf{g}_j is the solution to the linear system

$$A_h \mathbf{g}_i = \mathbf{e}_i, \quad (93)$$

and also satisfies the estimate

$$|\mathbf{g}_i|_\infty \equiv \max_{1 \leq j \leq N} |g_i(\mathbf{p}_j)| \leq C |\log h| \quad (94)$$

in the discrete maximum norm.

Now we are ready to prove Theorem 6.

Proof. [Theorem 6] Assume that

$$D_h^{-1} A_h (u_{v,h}(\mathbf{p}_i) - u_v(\mathbf{p}_i)) = E_i, \quad (95)$$

for $i = 1, 2, \dots, N$, with $E_i = O(h^2)$ if \mathbf{p}_i is a regular grid node and $E_i = O(h)$ if \mathbf{p}_i is irregular. Let

$$\mathcal{J}^* \equiv \{i: \mathbf{p}_i \text{ is irregular grid node.}\} \quad (96)$$

be the set of indices of irregular grid nodes. By the assumption that the number of irregular grid nodes is on the order of hN , we have $|\mathcal{J}^*| = C_0 N h$ for some $C_0 > 0$. Let $\mathbf{E}_h \equiv (E_1, E_2, \dots, E_N)^T$. From error equation (95), we get

$$u_{v,h}(\mathbf{p}_i) - u_v(\mathbf{p}_i) = (A_h^{-1} D_h \mathbf{E}_h)_i. \quad (97)$$

For simplicity, assume that each entry in the diagonal of the matrix D_h is equal to h^2 . Let

$$E^* \equiv \max_{j \in \mathcal{J}^*} |E_j| = C_1 h \text{ and } E^{**} \equiv \max_{j \notin \mathcal{J}^*} |E_j| = C_2 h^2. \text{ From (97), we could further obtain}$$

$$|u_{v,h}(\mathbf{p}_i) - u_v(\mathbf{p}_i)| \leq h^2 \sum_{j=1}^N |g_{i,j} E_j| \leq h^2 \left\{ \sum_{j \in \mathcal{J}^*} g_{i,j} E^* + \sum_{j \notin \mathcal{J}^*} g_{i,j} E^{**} \right\} \leq h^2 \left\{ C_1 h \sum_{j \in \mathcal{J}^*} g_{i,j} + C_2 h^2 \sum_{j \notin \mathcal{J}^*} g_{i,j} \right\} \leq h^2 \{ C_1 h |\mathcal{J}^*| + C_2 h^2 N \} |g_i|_\infty \leq C(C_1 + C_2) h^2 |\log h|. \quad (98)$$

10 Interpolation of the Volume and Boundary Integrals

As in general the Green's function $G(\mathbf{p}; \mathbf{q})$ of the elliptic operator \mathcal{L} in the regular domain \mathcal{Q} is not analytically available, we replace step (22a) (or (23a) for Neumann BVPs) with the corrected linear system (49). That is, given the approximate jump $\mu_{\nu}(\mathbf{p})$, we could first compute the corrections $C_{\nu,h}$, next solve the linear system (49) and denote the approximate solution by $u_{\nu,h}(\mathbf{p})$. Then we extract the limit values of $u_{\nu,h}^+(\mathbf{p})$ (from inside) (or its flux for Neumann BVPs) using Taylor expansions of the approximate solution $u_{\nu,h}$ around the discretization nodes of the boundary curve (see Fig. 4).

We treat the approximate solution $u_{\nu,h}(\mathbf{p})$ as a piecewise smooth function even though only the values of the function at the grid nodes are known. Assume the function and its derivatives are possibly discontinuous only on the domain boundary Ω . We also assume

that the approximate solution $u_{v,h}(\mathbf{p})$ is smooth enough in $\mathcal{A} \setminus \Omega$ such that the action of the continuous operator \mathcal{L} on it is meaningful.

Taylor expansion of the approximate solution $u_{v,h}(\mathbf{p})$ around a point \mathbf{q} on the domain boundary Ω (see Fig. 4) gives us

$$u_{v,h}(\mathbf{p}) = \mathbf{u}_{v,h}^+(\mathbf{q}) + \frac{\partial \mathbf{u}_{v,h}^+(\mathbf{q})}{\partial \mathbf{x}} \xi + \frac{\partial \mathbf{u}_{v,h}^+(\mathbf{q})}{\partial \mathbf{y}} \eta + \frac{1}{2} \frac{\partial^2 \mathbf{u}_{v,h}^+(\mathbf{q})}{\partial \mathbf{x}^2} \xi^2 + \frac{\partial^2 \mathbf{u}_{v,h}^+(\mathbf{q})}{\partial \mathbf{x} \partial \mathbf{y}} \xi \eta + \frac{1}{2} \frac{\partial^2 \mathbf{u}_{v,h}^+(\mathbf{q})}{\partial \mathbf{y}^2} \eta^2 + \mathbf{O}(|\mathbf{p} - \mathbf{q}|^3) \text{ if } \mathbf{p} \in \Omega, \quad (99)$$

and

$$u_{v,h}(\mathbf{p}) = \mathbf{u}_{v,h}^-(\mathbf{q}) + \frac{\partial \mathbf{u}_{v,h}^-(\mathbf{q})}{\partial \mathbf{x}} \xi + \frac{\partial \mathbf{u}_{v,h}^-(\mathbf{q})}{\partial \mathbf{y}} \eta + \frac{1}{2} \frac{\partial^2 \mathbf{u}_{v,h}^-(\mathbf{q})}{\partial \mathbf{x}^2} \xi^2 + \frac{\partial^2 \mathbf{u}_{v,h}^-(\mathbf{q})}{\partial \mathbf{x} \partial \mathbf{y}} \xi \eta + \frac{1}{2} \frac{\partial^2 \mathbf{u}_{v,h}^-(\mathbf{q})}{\partial \mathbf{y}^2} \eta^2 + \mathbf{O}(|\mathbf{p} - \mathbf{q}|^3) \text{ if } \mathbf{p} \in \Omega^c, \quad (100)$$

Here, $(\xi, \eta)^T = \mathbf{p} - \mathbf{q}$. For conciseness, we denote the limit values of the approximate solution $u_{v,h}$ and its derivatives by

$$V^\pm \equiv u_{v,h}^\pm(\mathbf{q}), \mathbf{V}_x^\pm \equiv \frac{\partial \mathbf{u}_{v,h}^\pm(\mathbf{q})}{\partial \mathbf{x}}, \mathbf{V}_y^\pm \equiv \frac{\partial \mathbf{u}_{v,h}^\pm(\mathbf{q})}{\partial \mathbf{y}}, \quad (101)$$

and

$$V_{xx}^\pm \equiv \frac{\partial^2 u_{v,h}^\pm(\mathbf{q})}{\partial x^2}, V_{xy}^\pm \equiv \frac{\partial^2 u_{v,h}^\pm(\mathbf{q})}{\partial x \partial y}, V_{yy}^\pm \equiv \frac{\partial^2 u_{v,h}^\pm(\mathbf{q})}{\partial y^2}. \quad (102)$$

Some subscripts are omitted.

Evaluating the truncated Taylor series, (99) or (100), at six nearby grid nodes $\mathbf{p}_j (j = 0, 1, \dots, 5)$ (see Fig. 4) yields

$$V^+ + V_x^+ \xi_j + V_y^+ \eta_j + \frac{1}{2} \xi_j^2 V_{xx}^+ + \xi_j \eta_j V_{xy}^+ + \frac{1}{2} \eta_j^2 V_{yy}^+ = V_j \text{ if } \mathbf{p}_j \in \Omega \quad (103)$$

and

$$V^- + V_x^- \xi_j + V_y^- \eta_j + \frac{1}{2} \xi_j^2 V_{xx}^- + \xi_j \eta_j V_{xy}^- + \frac{1}{2} \eta_j^2 V_{yy}^- = V_j \text{ if } \mathbf{p}_j \in \Omega^c, \quad (104)$$

with $V_j \equiv u_{v,h}(\mathbf{p}_j)$ and $(\xi_j, \eta_j)^T = \mathbf{p}_j - \mathbf{q}$, for $j = 0, 1, \dots, 5$. Let

$$J_j \equiv [V] + \xi_j [V_x] + \eta_j [V_y] + \frac{1}{2} \xi_j^2 [V_{xx}] + \xi_j \eta_j [V_{xy}] + \frac{1}{2} \eta_j^2 [V_{yy}]. \quad (105)$$

Using the jump relations of the solution and its derivatives, we rewrite (104) as

$$V^+ + V_x^+ \xi_j + V_y^+ \eta_j + \frac{1}{2} \xi_j^2 V_{xx}^+ + \xi_j \eta_j V_{xy}^+ + \frac{1}{2} \eta_j^2 V_{yy}^+ = V_j + j_j \text{ if } p_j \in \Omega^c. \quad (106)$$

Let $a_j \equiv \xi_j/h$, $b_j \equiv \eta_j/h$ and introduce new quantities:

$$W^\pm \equiv V^\pm, W_a^\pm \equiv h V_x^\pm, W_b^\pm \equiv h V_y^\pm, \quad (107)$$

and

$$W_{aa}^\pm \equiv h^2 V_{xx}^\pm, W_{ab}^\pm \equiv h^2 V_{xy}^\pm, W_{bb}^\pm \equiv h^2 V_{yy}^\pm. \quad (108)$$

Then from Eqns. (103) and (106), we obtain

$$W^+ + a_j W_a^+ + b_j W_b^+ + \frac{1}{2} a_j^2 W_{aa}^+ + a_j b_j W_{ab}^+ + \frac{1}{2} b_j^2 W_{bb}^+ = V_j \text{ if } p_j \in \Omega \quad (109)$$

or

$$W^+ + a_j W_a^+ + b_j W_b^+ + \frac{1}{2} a_j^2 W_{aa}^+ + a_j b_j W_{ab}^+ + \frac{1}{2} b_j^2 W_{bb}^+ = V_j + J_j \text{ if } p_j \in \Omega^c \quad (110)$$

for $j = 0, 1, \dots, 5$. Note that the coefficient matrix of (109)-(110) is independent of the mesh parameter h . The limit values of the approximate solution and its derivatives are uniquely determined by (109)-(110) if we appropriately choose the the six grid nodes \mathbf{p}_j ($j = 0, 1, \dots, 5$) such that the coefficient matrix is invertible.

In the case that the structured grid consists of rectangular or quadrilateral elements, we chose an interpolation stencil as the nearest six grid nodes, which looks like a fish but never being a two by three rectangle, and four of which are the vertices of the element that contains the curve node \mathbf{q} in its interior (see Fig. 4(a)). In the case that the structured grid consists of triangular elements, we choose the six grid nodes such that the stencil forms a triangle, which contains in its interior the curve node \mathbf{q} of interest on the boundary curve (see Fig. 4(b)). With interpolation nodes chosen as above, the matrix is always invertible and the polynomial interpolation scheme is guaranteed to be stable ([26,72]).

11 Numerical Results

Numerical results from application of the kernel free boundary integral method to solving BVPs with either Neumann or Dirichlet boundary conditions are presented in this section.

To study the convergence rate and efficiency of the KFBI method, in the numerical simulations for each test problem, the boundary curve Ω and the regular domain \mathcal{Q} , into which the original complex domain Ω is embedded, are simultaneously refined with a refinement ratio of two.

In the numerical experiments reported in this section, the GMRES iterative method is used to solve the boundary integral equations. For Dirichlet BVPs, the unknown density is initialized as $\varphi_0 = 2g^D$; for Neumann BVPs, the unknown density is initialized as $\psi_0 = 2g^N$. The GMRES iteration stops only when the relative residual in a scaled discrete ℓ^2 -norm is less than a small tolerance, i.e.,

$$\frac{\|\bar{g}_h^D - \bar{K}\varphi_{v,h}\|_2}{\|\bar{g}_h^D\|_2} < \epsilon_{tol} \quad (111)$$

for the boundary integral equation (24) corresponding to the Dirichlet BVPs and

$$\frac{\|\bar{g}_h^N - \bar{K}^*\psi_{v,h}\|_2}{\|\bar{g}_h^N\|_2} < \epsilon_{tol} \quad (112)$$

for the boundary integral equation (26) corresponding to the Neumann BVPs. In the simulations presented, the tolerance is fixed to be

$$\epsilon_{tol} \equiv 10^{-6} \quad (113)$$

The scaled discrete ℓ^2 -norm of a vector $\mathbf{v} = (v_1, v_2, \dots, v_n)^T \in \mathbb{R}^n$ is defined by

$$\|\mathbf{v}\|_2 \equiv \sqrt{\frac{1}{n} \sum_{i=1}^n v_i^2}. \quad (114)$$

In the first three test problems, the regular domain \mathcal{Q} is chosen to be the rectangular box $\mathcal{Q} = (-1, 1)^2$ and the diffusion tensor and the reaction coefficient of the elliptic operator are assumed to be isotropic and homogeneous. That is, we first consider solving the constant coefficients BVPs on complex domains (see Fig. 1). In these cases, the elliptic operator \mathcal{L} degenerates to be the Laplacian operator ($\kappa = 0$) or the generalized Helmholtz operator ($\kappa > 0$). The corresponding interface problems on Cartesian grids are simply discretized by the five-point central finite difference scheme and solved with a FFT-based Poisson (Helmholtz) solver.

Numerical results for the first two test problems are summarized in Tables 1-2 and Figs. 5-6. In each of the tables, the first column contains the numbers of nodes on Ω , denoted by M_Ω , which are used to discretize the boundary curves. The second column contains the sizes of the Cartesian grids used to solve the interface problems. The other columns are respectively the errors of the data in the scaled discrete ℓ^2 -norm ($\|e_h\|_2$) and the maximum norm ($\|e_h\|_\infty$) and the number of GMRES iterations (ν). In the tables, the number of GMRES iterations is also the times the FFT-based fast Poisson (Helmholtz) solver is called during the simulation.

Example 1 (An interior Dirichlet BVP on a star-shaped domain)

The boundary curve of the star-shaped domain is defined by

$$x(\theta) = 0.6(1 + 0.25\sin 6\theta)\cos\theta, \quad (115)$$

$$y(\theta) = 0.6(1 + 0.25\sin 6\theta)\sin\theta, \quad (116)$$

for $\theta \in [0, 2\pi)$, which is completely contained in the rectangular box $B = (-1, 1)^2$. The Dirichlet boundary conditions on Ω are chosen such that the exact solution to the problem is given by

$$u(x, y) = x^3 - y^3. \quad (117)$$

The boundary conditions on \mathcal{B} are simply set as zero. See Table 1 for the errors and Fig. 5 for the numerical solution on a 128×128 grid.

Example 2 (An interior Neumann BVP on a heart-shaped domain)

The boundary curve Ω is fitted with a cubic spline. Pure Neumann boundary conditions are applied on Ω such that the exact solution is given by

$$u(x, y) = \sin \frac{\pi x}{2} \sin \frac{\pi y}{2}. \quad (118)$$

The boundary conditions on \mathcal{B} are simply set as zero. In the case that the reaction coefficient vanishes ($\kappa = 0$), the solution to the pure Neumann BVP is not unique but only up to an additive constant. To compute numerical errors, we translate the solution to the corresponding interface problem by a constant such that the numerical solution matches the exact one at the center of the box B. See Table 2 for the errors and Fig. 6 for the numerical solution on a 128×128 grid.

The numerical results presented in Tables 1-2 uniformly verify that the Cartesian grid method proposed is of second-order accurate. The number of GMRES iterations used for the boundary integral equations is independent of the grid size, which is in contrast to Wiegmann and Bube's explicit jump II method and Li and Ito's augmented strategies for constant coefficient BVPs.

In our experiments, simple iterations like (22) and (23) have also been correspondingly applied to solve the integral equations for Examples 1-2 with the same uniform grids of different sizes. We chose the iteration parameter β to be equal to 0.8 and used the same stopping criteria and tolerance as the GMRES iteration. It is observed that, for the interior Dirichlet BVP in Example 1, the iteration number used by the simple iteration (22) is 19 on the coarsest 64×64 grid and always 17 on others, more than those used by the GMRES method. For the interior Neumann BVP with non-vanishing reaction coefficient ($\kappa = 1$) in Example 2, the iteration number used by the simple iteration (23) is 46 on the coarsest 64×64 grid and always 47 on others. For the interior Neumann BVP with vanishing reaction coefficient ($\kappa = 0$) in Example 2, during each iteration, the iterated density is modified such that it has zero mean value, which guarantees the simple iteration converges for the singular integral equation; the iteration number used by the simple iteration is 26 on the coarsest 64×64 grid and always 27 on other grids.

Example 3 (A Neumann BVP on the complements of complex domains)

In this example, we solve the Laplace's equation with homogeneous Neumann boundary conditions on the boundaries Ω of two different complex domains (a mushroom-shaped domain and a spiral-shaped domain) (see Fig. 7) and Dirichlet boundary conditions on the boundary \mathcal{B} of the rectangular box, which say

$$g^D(x, y) = x \text{ on } \partial\mathcal{B}. \quad (119)$$

We run simulations with five grids of different resolutions ranging from 64×64 to 1024×1024 as before. It is observed that the iteration numbers used by the GMRES method for the

problem on the mushroom-shaped domain are always 24 while those on the spiral-shaped domain fluctuate between 35 and 36.

In the next two examples, we use the standard continuous piecewise bilinear finite element method to solve the interior Dirichlet/Neumann boundary value problems. Both isotropic and anisotropic BVPs are tested. In the anisotropic case, for simplicity, we assume the diffusion tensor is spatially uniform and has the form

$$\sigma = \begin{pmatrix} \cos\theta & -\sin\theta \\ \sin\theta & \cos\theta \end{pmatrix} \begin{pmatrix} \lambda_1 \\ \lambda_2 \end{pmatrix} \begin{pmatrix} \cos\theta & \sin\theta \\ -\sin\theta & \cos\theta \end{pmatrix}, \quad (120)$$

with $\lambda_1 = 1$, $\lambda_2 = 1/\mu$ and $\theta = \pi/4$. Here, $\mu > 1$ is the anisotropy ratio of the diffusion tensor. It ranges from two to a hundred. The larger regular domain B is still chosen to be the square rectangular box as above, i.e., $\mathcal{B} = (-1, 1)^2$. The box is partitioned into a hierarchy of Cartesian grids. The resulting linear systems are solved by a geometric multigrid solver (exactly, an implementation based on V -cycle preconditioned conjugate gradient iterations). In these simulations, we used the technique of mass lumping (row-sum) to assembly the mass matrices involved.

Numerical results for the test problems are summarized in Tables 3-7 and Figs. 8-9. In each of the tables, the first column contains the numbers of nodes on Ω , denoted by M_Ω , which are used to discretize the boundary curves. The second column contains the sizes of the Cartesian grids used to solve the interface problems. The other columns are respectively the errors of the data in the scaled discrete L^2 -norm ($\|e_h\|_2$) and the maximum norm ($\|e_h\|_\infty$) and the number of GMRES iterations (ν). In the tables, the number of GMRES iterations is also the times the geometric multigrid solver is called during the simulation.

Example 4 (An interior Dirichlet BVP on a circular domain)

The circular domain Ω is defined by

$$\left\{ (x, y)^T \mid \frac{x^2}{0.6^2} + \frac{y^2}{0.6^2} < 1 \right\}. \quad (121)$$

The reaction coefficient in the elliptic operator is fixed to be zero, i.e., $k = 0$. Pure Dirichlet boundary conditions are applied on Ω such that the exact solution is given by

$$u(x, y) = x^3 - y^3. \quad (122)$$

The boundary conditions on \mathcal{B} are simply set as zero. See Table 3 for the errors and Fig. 8 for the numerical solutions on a 128×128 grid.

Example 5 (An interior Neumann BVP on an ellipse-shaped domain)

The ellipse-shaped domain Ω is defined by

$$\left\{ (x, y)^T \mid \frac{x^2}{0.8^2} + \frac{y^2}{0.4^2} < 1 \right\}. \quad (123)$$

Pure Neumann boundary conditions are applied on Ω such that the exact solution is given by

$$u(x, y) = \sin \frac{\pi x}{2} \sin \frac{\pi y}{2}. \quad (124)$$

The boundary conditions on \mathcal{L} are simply set as zero. Both cases of zero and non-zero reaction coefficients, $k = 0$ and $k = 1$, are tested. In the case that $k = 0$, the solution to the pure Neumann BVP is not unique but only up to an additive constant. To compute numerical errors, we translate the solution to the corresponding interface problem by a constant such that the numerical solution matches the exact one at the center of the box \mathcal{L} . See Tables 5-7 for the errors and Fig. 9 for the numerical solutions on a 128×128 grid. Table 5 and Fig. 9 compare results for solving isotropic and moderately anisotropic Neumann BVPs. Table 6 shows the results from solving the pure Neumann problem with the reaction coefficient vanishing ($\kappa = 0$). Table 7 shows the results with a non-zero reaction coefficient ($\kappa = 1$).

The numerical results summarized in Tables 3-7 for the previous two examples indicate that, in the regime with strong anisotropy ratios of the diffusion tensor, the method for solving Dirichlet BVPs and Neumann boundary value Helmholtz problems ($\kappa = 0$) performs much better than for the pure Neumann BVPs, where the reaction coefficient is vanishing. For isotropic and moderately anisotropic BVPs, the numerical results were consistent with the theoretical expectation for both the accuracy and efficiency of the method.

Example 6 (Continued, the pure Neumann BVP on an ellipse-shaped domain)

To compare with the previous example and investigate the effect of the orientation of the diffusion tensor on the accuracy and efficiency of the method, in this example, we choose the diffusion tensor simply as

$$\sigma = \begin{pmatrix} \lambda_1 & \\ & \lambda_2 \end{pmatrix} \quad (125)$$

with $\lambda_1 = 1$, $\lambda_2 = 1/\mu > 1$ being the anisotropy ratio. In words, the diffusion tensor is aligned with the grid lines (coordinate axis). Other settings, including simulation parameters, boundary conditions and exact solutions, are the same as Example 5, except that the reaction coefficient is fixed to be zero ($\kappa = 0$). Numerical results are summarized in Table 8.

Table 8 shows that the results from the KFBI method are consistent with that predicted by the theoretical analysis when the diffusion tensor is aligned with the grid lines. Even for severely strong anisotropic Neumann BVPs, the method still shows its second-order convergence rate in accuracy and grid-independent iteration numbers when the grid is fine enough (size not less than 256×256 for the test problem).

12 Discussion

The KFBI method is stable and accurate for general (possibly anisotropic) elliptic boundary value problems. It employs a Krylov subspace method (the GMRES iteration) to compute the densities of the double or single layer potential from the boundary integral equation, corresponding to the Dirichlet or Neumann BVP. The Krylov subspace method is guaranteed to converge by the spectral properties of the double/single layer boundary integral operators. For isotropic and moderately anisotropic BVPs, it is observed that the number of GMRES iterations used is independent of the sizes of the grids employed. The

volume and boundary integrals, which are required by the GMRES iteration for updating the densities, are computed as limit values of the structured grid-based approximate solutions. Because analytical expressions of Green's functions are not required, the method is kernel-free.

In this work, only the details for a second-order implementation of the KFBI method in two dimensions are described. In principle, it is natural and straightforward to derive higher-order extensions of the method as long as the elliptic operator \mathcal{L} is discretized with a higher-order discretization scheme and the computation of the jumps of the derivatives, the correction of the source term and the approximation of the integrals employ more grid nodes and more terms in the Taylor series. While the extension of the method to higher space dimensions is also straightforward, the validity of the method for BVPs on domains with piece-wise smooth boundaries needs to be investigated.

The KFBI method is flexible as well as efficient. The regular domain \mathcal{G} can be chosen arbitrarily to be a triangle, a rectangle, a circle, a ring or any other regularly shaped domain as long as the Green's function on \mathcal{G} exists and fast elliptic solvers are readily applicable. Additionally, it is important to know that the numerical solutions on the structured grids can be obtained by a variety of discretization methods.

Because the method does not modify the stiffness matrix, which results from the discretization of the elliptic operator with a standard discretization scheme, a standard linear system solver such as the fast Fourier transform (FFT) based Poisson (Helmholtz) solvers or those based on geometric multigrid iterations can be easily combined. For time-dependent problems, the KFBI method also has its advantage against those modifying matrices in each timestep. Moreover, the KFBI method allows the edges adjacent to an irregular node to intersect with the boundary of the complex domain several times. It has potential to work with coarse grids even though the boundary curve is "very close to itself".

The extension of the KFBI method for BVPs on multiply connected bounded domains will be studied in the near future. As the standard boundary integral equation corresponding to a BVP on a multiply connected domain is singular, some additional techniques have to be used for the KFBI method to be applicable. One strategy is to add singular sources through introducing (regularized) delta function(s) [17] into the source term of the BVP. An alternative one is to incorporate the explicit jump concept by Wiegmann and Bube [26].

As the spectrum of the boundary integral operators is contained in the interval $(-1/2, 1/2)$, iterative methods even as simple as (22) and (23) will converge as long as the structured grids used to compute the approximate solutions are sufficiently fine. The convergence rate, however, may deteriorate in some situations when the shape of the domain is not simple since the eigenvalues are closely clustered around the endpoints of the interval $(-1/2, 1/2)$. As indicated by the numerical results from Example 3, the numbers of iterations used by the GMRES method for problems on the mushroom-shaped and spiral-shaped domains are respectively twice and three times those on simpler domains. To overcome the problem, an appropriate preconditioner for the GMRES method should be pursued.

Finally the method can be applied to anisotropic BVPs if the anisotropy ratio is not too strong. For strong anisotropy that is not aligned with the grid, the accuracy of the method may degrade. The loss of accuracy is more obvious when the method is used to solve pure Neumann BVPs with a vanishing reaction coefficient ($\kappa = 0$). The explicit relationship between the anisotropy ratio, the orientation of the diffusion tensor, the type of boundary conditions, the mesh parameter and error estimates is interesting and requires further study.

The KFBI method presented here can be applied to a wide range of elliptic boundary value problems that arise from the fields of fluid dynamics, material science and biophysics, including reaction diffusion modeling in cardiac and neuro-electrophysiology. While some limitations exist, the KFBI method is straightforward to implement and has demonstrated some advantages over other existing structured (Cartesian) grid methods.

Acknowledgments

The first author thanks John A. Trangenstein for his guidance during the author's Ph.D. studies. In particular, this work would never become possible without the studies from and the discussions with J. Thomas Beale. The kernel-free boundary integral method was motivated by the authors' joint work with J. Thomas Beale on a fast multipole accelerated high-order accurate boundary integral method. Finally, the authors thank the referees for their helpful comments.

References

1. Thomée V. From finite differences to finite elements: A short history of numerical analysis of partial differential equations. *J Comput Appl Math.* 2001; 128(1-2):1–54.
2. Liu GR, Gershwil ME, Lucas AM. *Mesh Free Methods.* CRC Press. 2002
3. Li S, Liu WK. *Meshfree Particle methods.* Berlin: Springer Verlag. 2004
4. Belytschko T, Chen JS. *Meshfree and Particle Methods.* John Wiley and Sons Ltd. 2007
5. Peskin CS. Numerical analysis of blood flow in the heart. *J Comput Phys.* 1977; 25:220–252.
6. Peskin CS. Lectures on mathematical aspects of physiology. *Lectures in Appl Math.* 1981; 19:69–107.
7. Peskin CS. The immersed boundary method. *Acta Numer.* 2002:1–39.
8. LeVeque RJ, Li ZL. The immersed interface method for elliptic equations with discontinuous coefficients and singular sources. *SIAM J on Num Anal.* 1994; 31(4):1019–1044.
9. Osher S, Sethian JA. Fronts propagating with curvature-dependent speed: algorithms based on hamilton-jacobi formulations. *J Comput Phys.* 1988; 79:12–49.
10. Fedkiw RP, Aslam T, Merriman B, Osher S. A non-oscillatory Eulerian approach to interfaces in multimaterial flows (the ghost fluid method). *J Comput Phys.* 1999; 152:457–492.
11. Liu XD, Fedkiw RP, Kang M. A boundary condition capturing method for Poisson's equation on irregular domains. *J Comput Phys.* 2000; 160:151–178.
12. Liu XD, Sideris TC. Convergence of the ghost fluid method for elliptic equations with interfaces. *Mathematics of Computation.* 2003; 72(244):1731–1746.
13. Mayo A. The fast solution of Poisson's and the biharmonic equations on irregular regions. *SIAM J Numer Anal.* 1984; 21:285–299.
14. Mayo A. Fast high order accurate solution of Laplace's equation on irregular regions. *SIAM J Sci Statist Comput.* 1985; 6:144–157.
15. Cortez R, Minion M. The blob projection method for immersed boundary problems. *J Comput Phys.* 2000; 161(2):428–453.
16. Lai MC, Peskin CS. An immersed boundary method with formal second-order accuracy and reduced numerical viscosity. *J Comput Phys.* 2000; 160:705–719.
17. Tornberg AK, Engquist B. Regularization techniques for numerical approximation of PDEs with singularities. *Journal of Scientific Computing.* 2003; 19:527–552.
18. Tornberg AK, Engquist B. Numerical approximations of singular source terms in differential equations. *J Comput Phys.* 2004; 200:462–488.
19. Engquist B, Tornberg AK, Tsai R. Discretization of Dirac delta functions in level set methods. *J Comput Phys.* 2005; 207:28–51.
20. Gibou F, Fedkiw RP. A fourth order accurate discretization for the Laplace and heat equations on arbitrary domains, with applications to the Stefan problem. *J Comput Phys.* 2005; 202:577–601.
21. Linnick MN, Fasel HF. A high-order immersed interface method for simulating unsteady incompressible flows on irregular domains. *J Comput Phys.* 2005; 204:157–192.

22. Li ZL, Ito K. Maximum principle preserving schemes for interface problems with discontinuous coefficients. *SIAM J Sci Comput.* 2001; 23(1):330–361.
23. Adams L, Li ZL. The immersed interface/multigrid methods for interface problems. *SIAM J Sci Comput.* 2002; 24(2):463–479.
24. Adams L, Chartier TP. New geometric immersed interface multigrid solvers. *SIAM J Sci Comput.* 2004; 25:1516–1533.
25. Li ZL. A fast iterative algorithm for elliptic interface problems. *SIAM J Numer Anal.* 1998; 35(1): 230–254.
26. Wiegmann A, Bube KP. The explicit-jump immersed interface method: finite difference methods for PDEs with piecewise smooth solutions. *SIAM J Numer Anal.* 2000; 37(3):827–862.
27. Li ZL, Wang WC, Chern IL, Lai MC. New formulations for interface problems in polar coordinates. *SIAM J Sci Comput.* 2003; 25:224–245.
28. Li ZL. A note on immersed interface method for three-dimensional elliptic equations. *Comput Math Applic.* 1996; 31(3):9–17.
29. LeVeque RJ, Li ZL. Immersed interface method for Stokes flow with elastic boundaries or surface tension. *SIAM J Sci Statist Comput.* 1997; 18:709–735.
30. LeVeque RJ, Zhang C. Immersed interface methods for wave equations with discontinuous coefficients. *Wave Motion.* 1997; 25:237–263.
31. Li ZL. Immersed interface method for moving interface problems. *Numerical Algorithms.* 1997; 14:269–293.
32. Fogelson AL, Keener JP. Immersed interface methods for Neumann and related problems in two and three dimensions. *SIAM J Sci Comput.* 2000; 22:1630–1654.
33. Li ZL, Lai MC. The immersed interface method for the Navier-Stokes equations with singular forces. *J Comput Phys.* 2001; 171:822–842.
34. Dumett M, Keener J. An immersed interface method for anisotropic elliptic problems on irregular domains in 2D. *Num. Methods Partial Differential Eqs.* 2005; 21:397–420.
35. Dumett MA, Keener JP. An immersed interface method for solving anisotropic elliptic boundary value problems in three dimensions. *SIAM J Sci Comput.* 2003:348–367.
36. Hou S, Liu XD. A numerical method for solving variable coefficient elliptic equation with interfaces. *J Comput Phys.* 2005; 202:411–445.
37. Mayo A. The rapid evaluation of volume integrals of potential theory on general regions. *J Comput Phys.* 1992; 100:236–245.
38. Mayo A, Greenbaum A. Fast parallel iterative solution of Poisson's and biharmonic equations on irregular regions. *SIAM J Sci Statist Comput.* 1992; 13:101–118.
39. Greenbaum A, Greengard L, Mayo A. On the numerical solution of the biharmonic equation in the plane. *Phys D.* 1992; 60:216–225.
40. Greenbaum A, Greengard L, McFadden GB. Laplace's equation and the Dirichlet-Neumann map in multiply connected domains. *J Comput Phys.* 1993; 105(2):267–278.
41. Beale JT, Lai MC. A method for computing nearly singular integrals. *SIAM J Numer Anal.* 2001; 38(6):1902–1925.
42. Beale JT. A grid-based boundary integral method for elliptic problems in three-dimensions. *SIAM J Numer Anal.* 2004; 42:599–620.
43. McKenney A, Greengard L, Mayo A. A fast Poisson solver for complex geometries. *J Comput Phys.* 1995; 118:348–355.
44. Berthelsen PA. A decomposed immersed interface method for variable coefficient elliptic equations with non-smooth and discontinuous solutions. *J Comput Phys.* 2004; 197:364–386.
45. Zhou YC, Zhao S, Feig M, Wei GW. High order matched interface and boundary method for elliptic equations with discontinuous coefficients and singular sources. *J Comput Phys.* 2006; 213(1):1–30.
46. Johansen H, Colella P. A Cartesian grid embedding boundary method for Poisson's equation on irregular domains. *J Comput Phys.* 1998; 147:60–85.
47. McCorquodale P, Colella P, Johansen H. A Cartesian grid embedded boundary method for the heat equation on irregular domains. *J Comput Phys.* 2001; 173:620–635.

48. Tseng YH, Ferziger JH. A ghost-cell immersed boundary method for flow in complex geometry. *J Comput Phys.* 2003; 192:593–623.
49. Oevermann M, Klein R. A cartesian grid finite volume method for elliptic equations with variable coefficients and embedded interfaces. *J Comput Phys.* 2006; 219:749–769.
50. Cahn JW, Hilliard JE. Free energy of a nonuniform system i. *J Chem Phys.* 1958; 28:258–267.
51. Proskurowski W, Widlund O. On the numerical solution of Helmholtz's equation by the capacitance matrix method. *Math Comp.* 1976; 30:433–468.
52. Calhoun D. A Cartesian grid method for solving the two-dimensional streamfunction-vorticity equations in irregular regions. *J Comput Phys.* 2002; 176:231–275.
53. Saad Y, Schultz MH. GMRES: A generalized minimal residual method for solving nonsymmetric linear systems. *SIAM J Sci Statist Comput.* 1986; 7:856–869.
54. Saad Y. *Iterative methods for sparse linear systems.* PWS Publishing Company, Boston. 1996
55. Kellogg OD. *Foundations of Potential Theory.* Springer-Verlag. 1929
56. Colton D. *Partial Differential Equations.* Random House, New York. 1988
57. Kress R. *Linear Integral Equations.* Springer-Verlag. 1989
58. Atkinson KE. *The Numerical Solution of Integral Equations of the Second Kind.* Cambridge University Press, Cambridge, UK. 1997
59. McLean W. *Strongly Elliptic Systems and Boundary Integral Equations.* Cambridge University Press. 2000
60. Bramble JH, Osborn JE. Rate of convergence estimates for nonselfadjoint eigenvalue approximations. 1973; 27(123):525–549.
61. Atkinson K. Convergence rates for approximate eigenvalues of compact integral operators. 1975; 12(2):213–222.
62. Osborn JE. Spectral approximation for compact operators. *Math Comp.* 1975; 29(131):712–725.
63. Strang G, Fix GJ. *An Analysis of the Finite Element Method.* Prentice-Hall. 1973
64. Oden JT, Reddy TN. *An Introduction to the Mathematical Theory of Finite Elements.* John Wiley and Sons, New York. 1976
65. Ciarlet PG. *The Finite Element Method for Elliptic Problems.* North-Holland. 1978
66. Hughes TJR. *The Finite Element Method: Linear Static and Dynamic.* Finite Element Analysis, Prentice-Hall. 1987
67. Zienkiewicz, OC.; Taylor, RL. *The Finite Element Method.* 4th. London, U.K.: McGraw-Hill; 1994.
68. Beale JT, Layton AT. On the accuracy of finite difference methods for elliptic problems with interfaces. *Commun Appl Math Comput Sci.* 2006; 1:91–119.
69. Rannacher R, Scott R. Some optimal error estimates for piecewise linear finite element approximations. *Math Comp.* 1982; 38:437–445.
70. Brenner SC, Scott LR. *The Mathematical Theory of Finite Element Methods.* Springer-Verlag. 1994
71. Bramble JH, Thomée V. Pointwise bounds for discrete Green's functions. *SIAM J Numer Anal.* 1969; 6:583–590.
72. Lorentz RA. *Multivariate Birkhoff interpolation.* Springer-Verlag, New York, NY. 1992

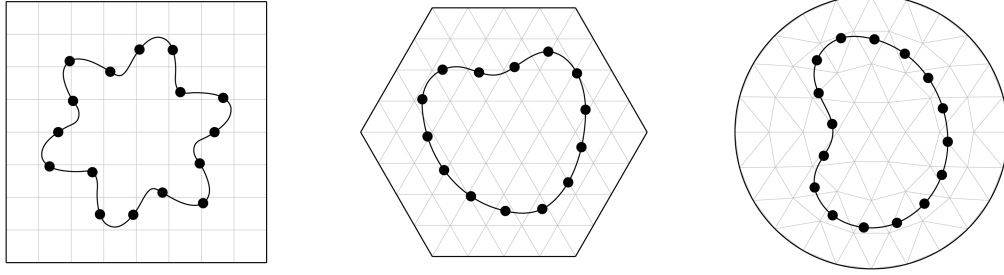


Fig. 1.

The kernel free boundary integral method assumes that the larger regular domain, which embeds the complex computational domain Ω , can be easily partitioned into a hierarchy of structured grids so that fast elliptic solvers such as the fast Fourier transform (FFT) based Poisson (Helmholtz) solvers or those based on geometric multigrid iterations are applicable. The boundary $\partial\Omega$ of the complex domain is partitioned into quasi-uniform curve segments. The number of the nodes on the curve is denoted by M_Ω . The values of the unknown densities φ_ν and ψ_ν are defined only at the M_Ω curve nodes. Other values of the densities and their tangential derivatives are reconstructed by a standard periodic twice continuously differentiable cubic spline.

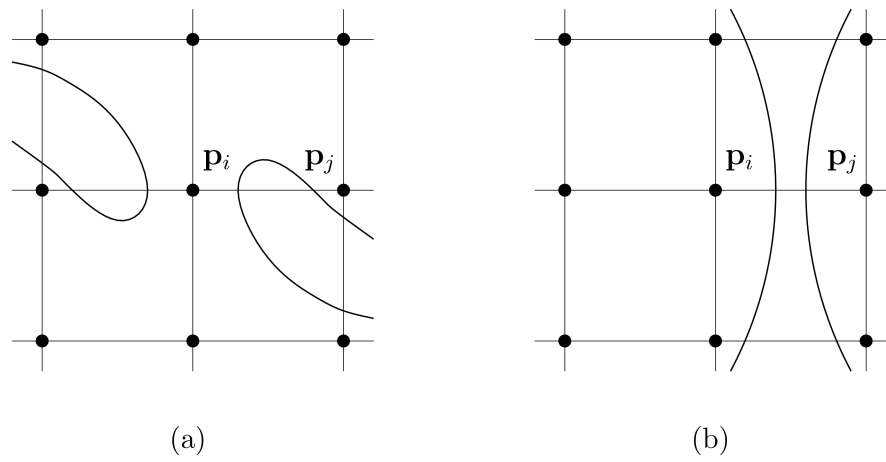


Fig. 2. The grid nodes p_j are irregular even though all of the nodes in the 9-point stencil are possibly on the same side of the boundary curve.

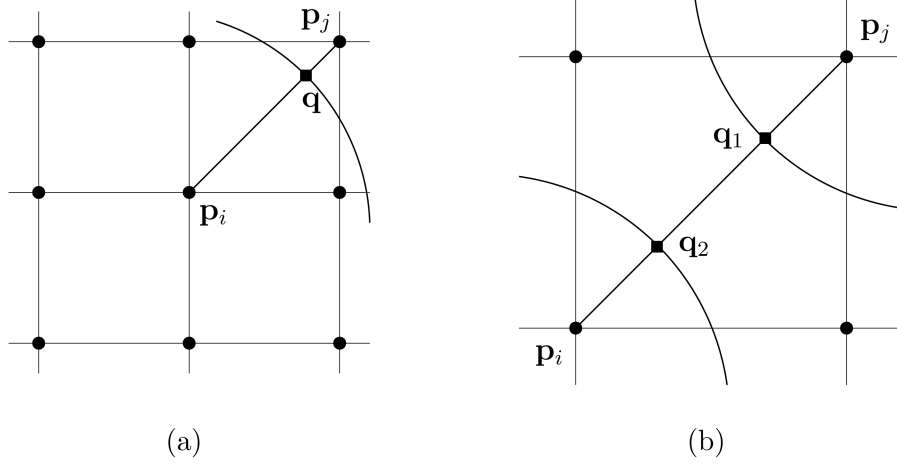


Fig. 3. The node p_i is irregular as the line segment connecting nodes p_i and p_j intersects with the boundary curve. The right hand side of the discrete linear system must be appropriately corrected at the irregular grid node. When the line segment intersects with the boundary curve several times, a multiplicative manipulation of the jumps is involved.

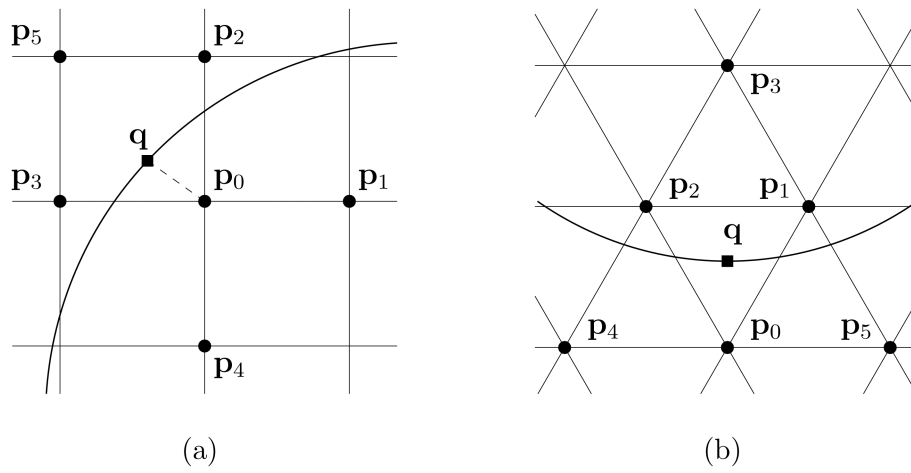


Fig. 4. Six grid nodes \mathbf{p}_j ($j=0,1, \dots,5$) for computing the limit values of an approximate solution and its derivatives at point \mathbf{q} .

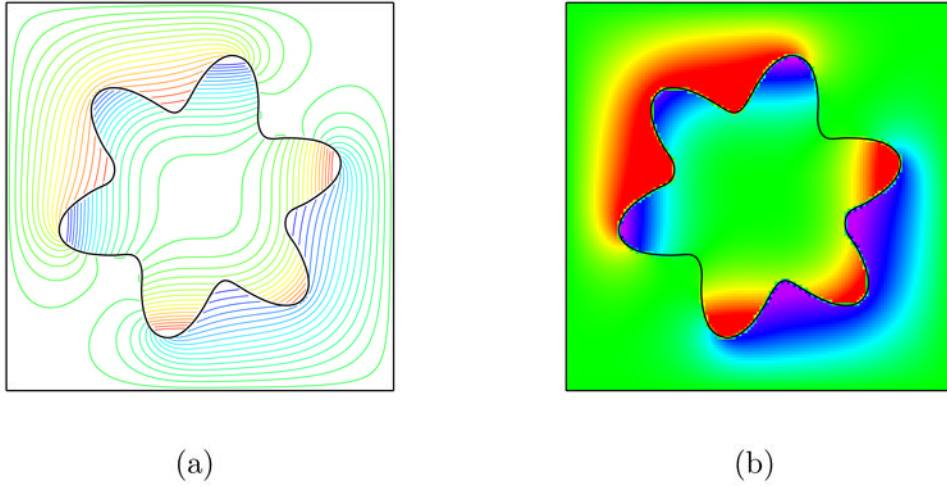


Fig. 5. Numerical solution to the interior Dirichlet boundary value problem on the star-shaped domain with a 128×128 grid (Example 1, $\kappa = 0$). In these two plots, the same iso-values and colormaps are used to visualize the interior and exterior data: maximum interior value of the solution $u_{max}^i = 0.369$, minimum interior value of the solution $u_{min}^i = -0.369$, maximum exterior value of the solution $u_{max}^e = 0.383$, minimum exterior value of the solution $u_{min}^e = -0.383$.

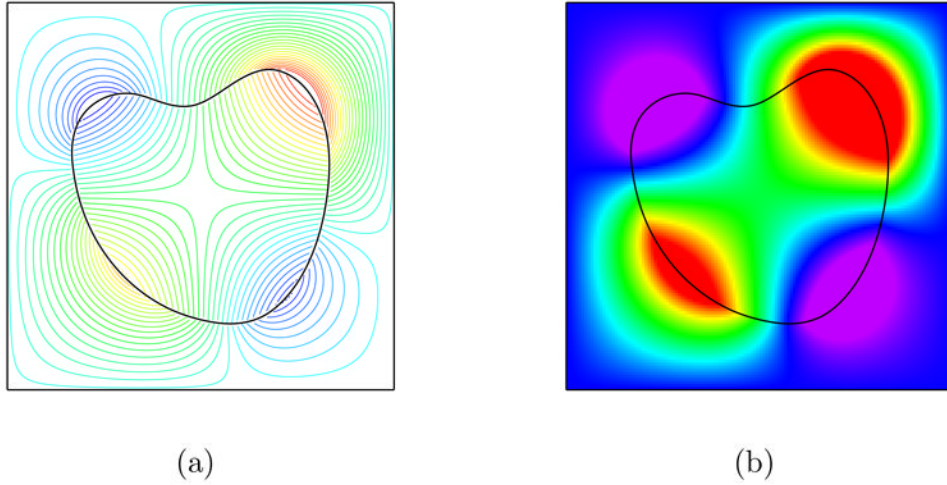


Fig. 6. Numerical solution to the interior Neumann boundary value problem on the heart-shaped domain with a 128×128 grid (Example 2, $\kappa = 0$). In these two plots, as the solution to the Neumann BVP is continuous across the domain boundary and both of the interior and exterior solutions achieve their maximum and minimum values on the boundary the same iso-values and colormaps are used to visualize the data: maximum interior value of the solution $u_{max}^i = 0.574$, minimum interior value of the solution $u_{min}^i = -0.519$, maximum exterior value of the solution $u_{max}^e = 0.564$, minimum exterior value of the solution $u_{min}^e = -0.514$.

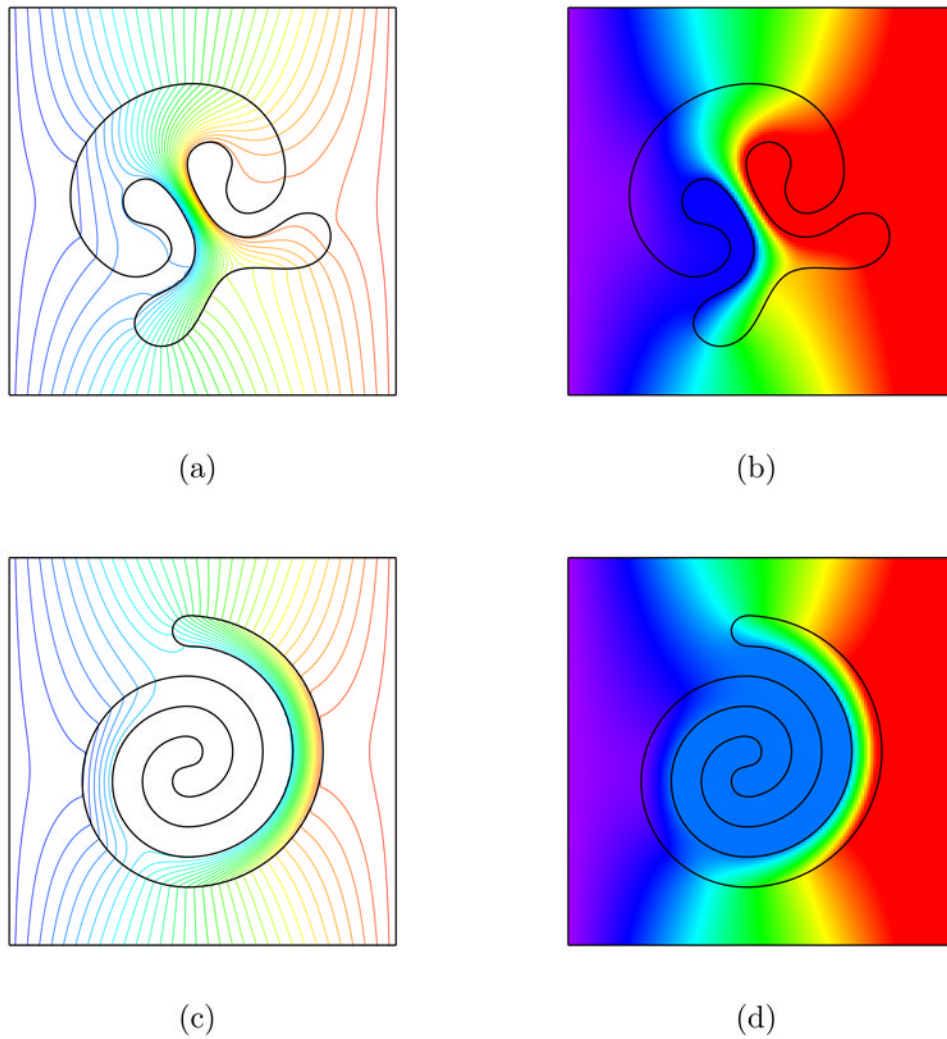


Fig. 7. The numerical solutions to the BVPs on the complements of complex domains with 128×128 grids (Example 3). Homogeneous Neumann boundary conditions are provided on the boundary of the complex domains. Dirichlet boundary conditions are provided on the boundary of the rectangular box. In the simulations with different grid sizes ranging from 64×64 to 1024×1024 , it is observed that the iteration numbers used by the GMRES method for the problem on the mushroom-shaped domain are straightly 24 while those on the spiral-shaped domain fluctuate between 35 and 36. In these figures, the interior and exterior data use the same isovalues and colormaps.

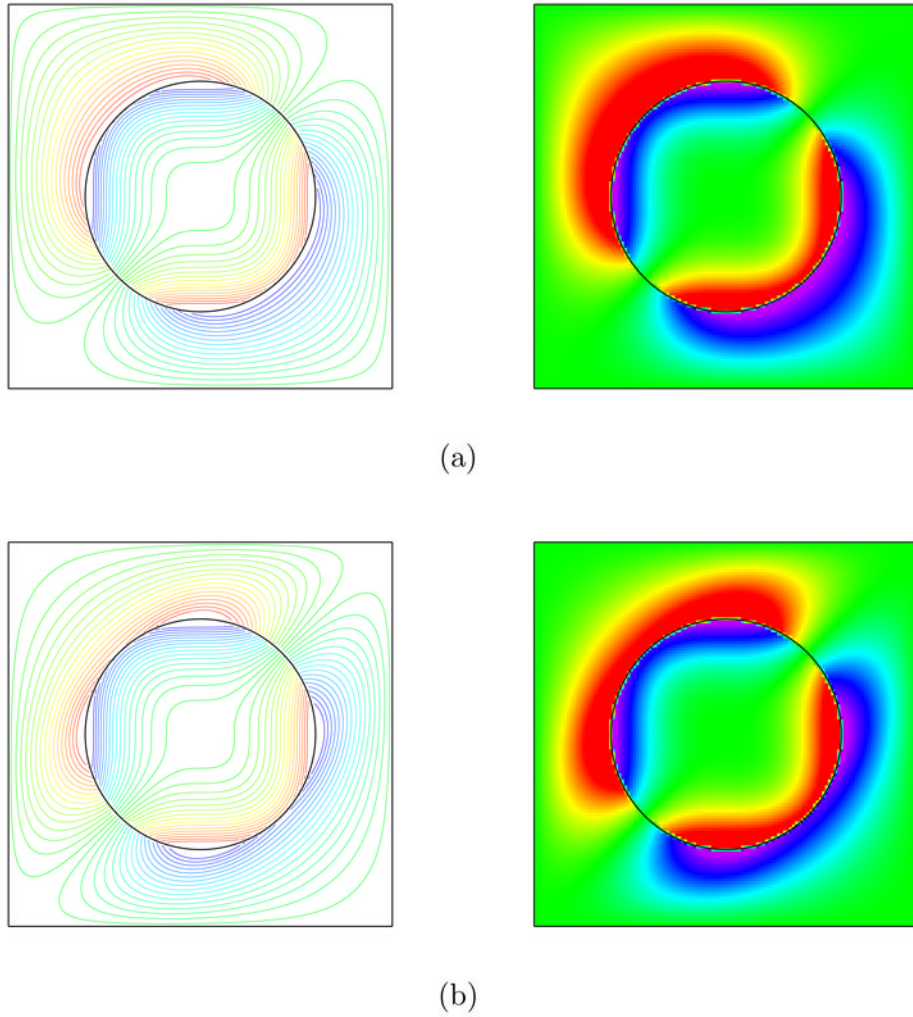


Fig. 8. Numerical solutions to the interior Dirichlet boundary value problem (Example 4) with the finite element method on a 128×128 grid: (a) the diffusion tensor is isotropic ($\sigma = 1$); (b) the diffusion tensor is anisotropic with anisotropy ratio 3: 1, the principle eigenvector aligned with the positive diagonal of the box \mathcal{B} .

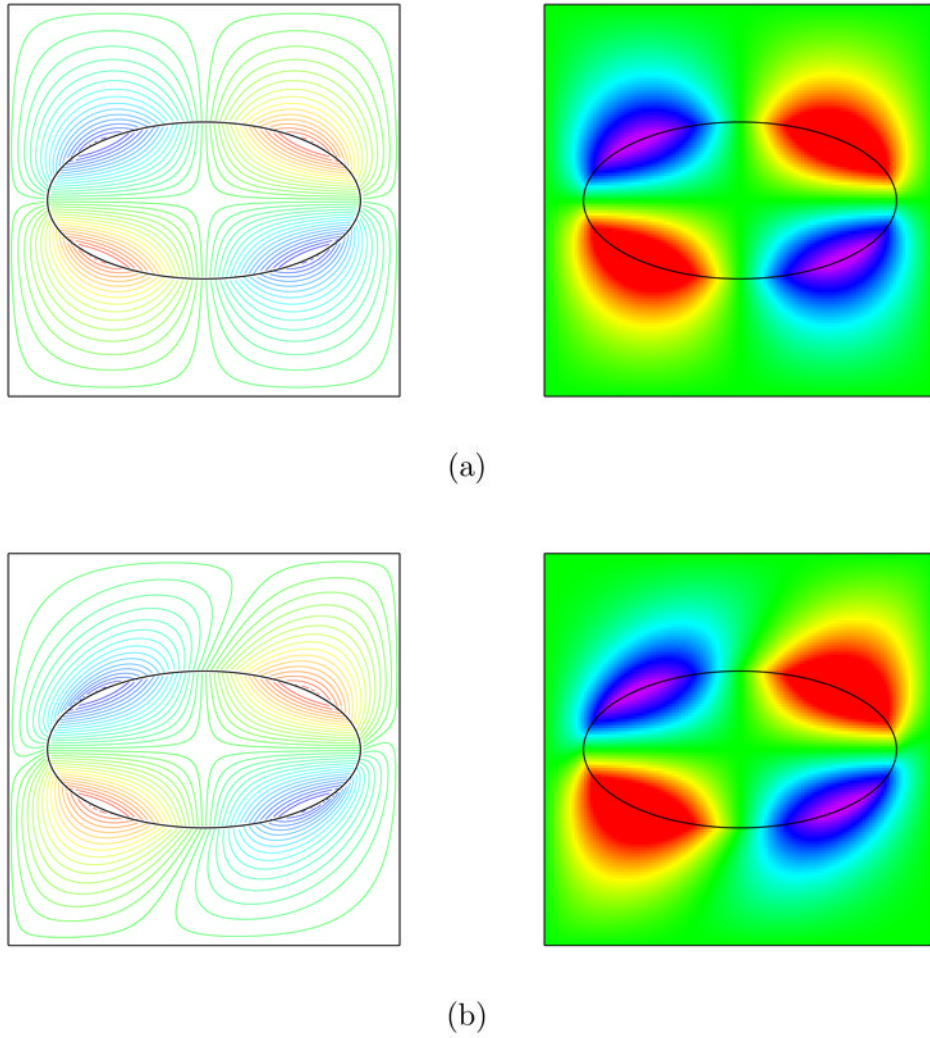


Fig. 9. Numerical solutions to the interior Neumann boundary value problem (Example 5, $\kappa = 1$) with the finite element method on a 128×128 grid: (a) the diffusion tensor is isotropic ($\sigma = 1$); (b) the diffusion tensor is anisotropic with anisotropy ratio 3: 1, the principle eigenvector aligned with the positive diagonal of the box \mathcal{Q} .

Table 1

Results from solving the interior Dirichlet BVP on the star-shaped domain (Example 1).

M	Ω	grid size	$\sigma=1, \kappa=0$			$\sigma=1, \kappa=1$		
			$\ e_h\ _2$	$\ e_h\ _{\infty}$	ν	$\ e_h\ _2$	$\ e_h\ _{\infty}$	ν
64		64×64	6.74E-5	7.89E-4	11	7.03E-5	8.48E-4	11
128		128×128	5.37E-6	8.64E-5	11	6.13E-6	8.88E-5	11
256		256×256	6.52E-7	1.54E-5	11	1.00E-6	1.54E-5	11
512		512×512	6.87E-8	4.38E-6	11	1.83E-7	5.48E-6	11
1024		1024×1024	1.05E-8	4.08E-7	11	4.16E-8	7.21E-7	11

Table 2

Results from solving the interior Neumann BVP on the heart-shaped domain (Example 2).

M	\mathbf{q}	$\sigma=1, \kappa=0$				$\sigma=1, \kappa=1$			
		$\ e_h\ _2$	$\ e_h\ _\infty$	ν	ν	$\ e_h\ _2$	$\ e_h\ _\infty$	ν	ν
56	64×64	$3.35E-4$	$1.30E-3$	12	12	$3.23E-4$	$1.40E-3$	10	10
112	128×128	$1.21E-4$	$5.04E-4$	13	13	$1.15E-4$	$4.08E-4$	10	10
224	256×256	$1.74E-5$	$8.97E-5$	13	13	$2.05E-5$	$6.66E-5$	10	10
448	512×512	$1.82E-6$	$1.53E-5$	14	14	$6.76E-6$	$1.65E-5$	10	10
896	1024×1024	$2.68E-7$	$4.55E-6$	14	14	$8.82E-7$	$3.04E-6$	10	10

Table 3

Results from solving the interior anisotropic Dirichlet BVP on the circular domain (Example 4, the diffusion tensor is aligned with the diagonals of the domain).

M	α_i	$\kappa = 0$		isotropic			anisotropy ratio 3:1		
		grid size	$\ e_h\ _2$	$\ e_h\ _{\infty}$	ν	$\ e_h\ _2$	$\ e_h\ _{\infty}$	ν	
30		64×64	$5.06E-5$	$4.13E-4$	6	$3.16E-5$	$2.43E-4$	6	
60		128×128	$1.65E-5$	$1.04E-4$	6	$1.03E-5$	$8.86E-5$	6	
120		256×256	$2.52E-6$	$3.20E-5$	6	$1.89E-6$	$1.74E-5$	6	
240		512×512	$8.17E-7$	$6.77E-6$	5	$5.43E-7$	$5.05E-6$	6	
480		1024×1024	$2.13E-7$	$2.14E-6$	5	$1.36E-7$	$1.29E-6$	6	

Table 4

More results from solving the anisotropic Dirichlet BVP on the circular domain (Example 4, the diffusion tensor is aligned with the diagonal of the domain).

M	α	$\kappa = 0$			anisotropy ratio 8:1			anisotropy ratio 20:1			
		grid size	$\ e_h\ _2$	$\ e_h\ _\infty$	ν	$\ e_h\ _2$	$\ e_h\ _\infty$	ν	$\ e_h\ _2$	$\ e_h\ _\infty$	ν
30		64×64	$9.07E-5$	$7.24E-4$	7	$4.64E-4$	$5.36E-3$	8	$4.64E-4$	$5.36E-3$	8
60		128×128	$1.62E-5$	$1.67E-4$	7	$1.25E-4$	$1.85E-3$	9	$1.25E-4$	$1.85E-3$	9
120		256×256	$4.02E-6$	$4.82E-5$	7	$3.25E-5$	$5.37E-4$	8	$3.25E-5$	$5.37E-4$	8
240		512×512	$1.18E-6$	$1.62E-5$	7	$9.35E-6$	$1.97E-4$	8	$9.35E-6$	$1.97E-4$	8
480		1024×1024	$2.88E-7$	$3.88E-6$	7	$2.34E-6$	$5.17E-5$	8	$2.34E-6$	$5.17E-5$	8

Table 5

Results from solving the interior anisotropic Neumann BVP on the ellipse-shaped domain (Example 5, the diffusion tensor is aligned with the diagonals of the domain).

$\kappa = 0$		isotropic			anisotropy ratio 3:1		
M	α	$\ e_h\ _2$	$\ e_h\ _{\infty}$	ν	$\ e_h\ _2$	$\ e_h\ _{\infty}$	ν
30	64×64	$2.13E-4$	$7.37E-4$	5	$6.03E-4$	$4.19E-3$	10
60	128×128	$2.72E-5$	$1.88E-4$	5	$3.89E-5$	$5.12E-4$	10
120	256×256	$8.30E-6$	$3.85E-5$	5	$1.02E-5$	$9.69E-5$	11
240	512×512	$2.10E-6$	$7.85E-6$	5	$3.10E-6$	$3.55E-5$	8
480	1024×1024	$4.77E-7$	$1.72E-6$	5	$4.79E-7$	$4.32E-6$	11

$\kappa = 1$		isotropic			anisotropy ratio 3:1		
M	α	$\ e_h\ _2$	$\ e_h\ _{\infty}$	ν	$\ e_h\ _2$	$\ e_h\ _{\infty}$	ν
30	64×64	$2.11E-4$	$7.37E-4$	5	$7.73E-4$	$2.96E-3$	8
60	128×128	$2.70E-5$	$1.90E-4$	5	$2.96E-4$	$6.58E-4$	7
120	256×256	$8.42E-6$	$3.89E-5$	5	$5.26E-5$	$1.92E-4$	8
240	512×512	$2.14E-6$	$7.98E-6$	5	$9.17E-6$	$4.14E-5$	8
480	1024×1024	$4.83E-7$	$1.75E-6$	4	$1.72E-6$	$3.51E-6$	8

Table 6

Results from solving the pure Neumann BVP on the ellipse-shaped domain (Example 5, $\kappa = 0$ and the diffusion tensor is aligned with the diagonals of the domain).

$\kappa = 0$		anisotropy ratio 8:1			anisotropy ratio 20:1		
M	α	$\ e_h\ _2$	$\ e_h\ _\infty$	ν	$\ e_h\ _2$	$\ e_h\ _\infty$	ν
30	64×64	6.18E-4	6.39E-3	10	1.71E-3	2.28E-2	11
60	128×128	1.57E-4	1.80E-3	11	1.11E-3	2.19E-2	13
120	256×256	3.86E-5	3.17E-4	13	1.81E-4	3.36E-3	16
240	512×512	2.56E-5	5.11E-4	13	2.62E-5	7.95E-4	16
480	1024×1024	4.15E-6	5.37E-5	14	6.90E-6	3.18E-4	18

Table 7

Results from solving the reaction-diffusion Neumann BVP on the ellipse-shaped domain (Example 5, $\kappa = 1$ and the diffusion tensor is aligned with the diagonals of the domain).

$\kappa = 1$		anisotropy ratio 8:1			anisotropy ratio 20:1		
M	Ω	$\ e_h\ _2$	$\ e_h\ _\infty$	ν	$\ e_h\ _2$	$\ e_h\ _\infty$	ν
30	64×64	1.66E-3	7.46E-3	9	4.23E-3	1.84E-2	9
60	128×128	4.88E-4	2.01E-3	8	1.49E-3	1.00E-2	11
120	256×256	4.01E-5	3.05E-4	9	3.96E-4	2.28E-3	11
240	512×512	4.97E-5	2.13E-4	9	1.59E-4	1.16E-3	10
480	1024×1024	5.97E-6	3.61E-5	9	1.18E-5	1.62E-4	10

Table 8

Results from solving the anisotropic pure Neumann BVP on the ellipse-shaped domain (Example 6, $\kappa = 0$ and the diffusion tensor is aligned with the coordinate axis).

M	α	$\kappa = 0$	anisotropy ratio 8:1			anisotropy ratio 20:1		
			$\ e_h\ _2$	$\ e_h\ _\infty$	ν	$\ e_h\ _2$	$\ e_h\ _\infty$	ν
30		64×64	$3.26E-4$	$1.68E-3$	6	$6.23E-4$	$2.89E-3$	8
60		128×128	$7.67E-5$	$3.99E-4$	6	$1.05E-4$	$7.44E-4$	7
120		256×256	$1.24E-5$	$9.43E-5$	6	$2.17E-5$	$2.15E-4$	7
240		512×512	$3.60E-6$	$2.57E-5$	6	$5.63E-6$	$6.85E-5$	7
480		1024×1024	$8.34E-7$	$6.29E-6$	6	$1.43E-6$	$1.79E-5$	7